The Company of **Biologists**

RESEARCH ARTICLE

SmcHD1 underlies the formation of H3K9me3 blocks on the inactive X chromosome in mice

Saya Ichihara[1], Koji Nagao[2,*], Takehisa Sakaguchi[3], Chikashi Obuse[2] and Takashi Sado[1,4,*]

ABSTRACT

Stable silencing of the inactive X chromosome (Xi) in female mammals is crucial for the development of embryos and their postnatal health. SmcHD1 is essential for stable silencing of the Xi, and its functional deficiency results in derepression of many X-inactivated genes. Although SmcHD1 has been suggested to play an important role in the formation of higher-order chromatin structure of the Xi, the underlying mechanism is largely unknown. Here, we explore the epigenetic state of the Xi in SmcHD1-deficient epiblast stem cells and mouse embryonic fibroblasts in comparison with their wild-type counterparts. The results suggest that SmcHD1 underlies the formation of H3K9me3-enriched blocks on the Xi, which, although the importance of H3K9me3 has been largely overlooked in mice, play a crucial role in the establishment of the stably silenced state. We propose that the H3K9me3 blocks formed on the Xi facilitate robust heterochromatin formation in combination with H3K27me3, and that the substantial loss of H3K9me3 caused by SmcHD1 deficiency leads to aberrant distribution of H3K27me3 on the Xi and derepression of X-inactivated genes.

KEY WORDS: X chromosome inactivation, Heterochromatin, Histone modifications

INTRODUCTION

X chromosome inactivation (XCI), a process by which the dosage imbalance of X-linked genes between the sexes in mammals is compensated for (Lyon, 1961), is a paradigm for understanding how chromatin organization is regulated. The noncoding *Xist* gene (Borsani et al., 1991; Brockdorff et al., 1991) on the X chromosome plays an indispensable role in the initiation of XCI (Marahrens et al., 1997; Penny et al., 1996). Transcriptional upregulation of *Xist* and the subsequent accumulation of the *Xist* transcript on the X chromosome from which it originates are thought to trigger stepwise processes of XCI involving epigenetic modifications. Immunofluorescence analyses have demonstrated that the inactive X chromosome (Xi) is enriched at histone H2A monoubiquitinated at lysine 119 (H2AK119ub) and histone H3 trimethylated at lysine 27 (H3K27me3) marks, the respective post-translational modifications of

which are catalyzed by Polycomb repressive complexes PRC1 and PRC2, respectively (Erhardt et al., 2003; Fang et al., 2004; Napoles et al., 2004; Plath et al., 2003; Silva et al., 2003). Species-specific differences in histone modifications on the Xi, however, have also been pointed out. Antibodies against histone H3 trimethylated at lysine 9 (H3K9me3) and H4 trimethylated at lysine 20 (H4K20me3) highlight the Xi in immunofluorescence assays in marsupials and some eutherians, including humans (Chadwick and Willard, 2004; Chaumeil et al., 2011; Rens et al., 2010; Zakharova et al., 2011), but their enrichments on the Xi are not evident in mice. This would partly explain why most studies of histone modifications in the mechanism of XCI have been focused on those mediated by PRC1 and PRC2 in mice. H3K9me3 and H4K20me3 are known to be enriched at sites of DAPI-dense constitutive heterochromatin, such as pericentromeric heterochromatin and telomeres in mammalian somatic cells (Peters et al., 2001; Schotta et al., 2004). A prevailing view is, therefore, that the mouse Xi is exceptional in that it may not share the mechanism used by the above-noted marsupials and eutherians to establish and maintain the repressed chromatin state with constitutive heterochromatin. A more recent study employing chromatin immunoprecipitation assays with sequencing (ChIP-seq), however, demonstrated that H3K9me3 was enriched on substantial regions of the Xi compared with the active X chromosome (Xa) in the mouse (Keniry et al., 2016).

Mutations of EED, one of the core components of PRC2 that is essential for PRC2-mediated production of H3K27me3, cause derepression of genes on the Xi in the trophoblast of the post-implantation mouse embryo, suggesting that H3K27me3 is not essential for the initiation of XCI, but is important for its maintenance (Kalantry and Magnuson, 2006; Kalantry et al., 2006; Montgomery et al., 2005; Wang et al., 2001). DNA methylation is also known to contribute to sustaining the inactivated state of the Xi (Mohandas et al., 1981). CpG islands (CGIs), which are often found in regulatory regions such as promoters and enhancers, are highly methylated on the Xi compared with those on the Xa. When cells are treated with DNA demethylating agents, such as 5-aza-cytidine, sporadic reactivation of previously silenced genes on the Xi often takes place in culture. Initiation of random XCI, by contrast, is not affected in the epiblast lineage of mouse embryos deficient for *de novo* DNA methyltransferases (Sado et al., 2004). These observations suggest that DNA methylation is dispensable for the initiation of XCI but plays a role in the maintenance of XCI. Another factor known to be involved in the maintenance of XCI is SmcHD1 (Blewitt et al., 2008). SmcHD1 is a noncanonical member of the SMC family of proteins and accumulates on the Xi. In female mouse embryos homozygous for a null mutation of *Smchd1*, *Smchd1MommeD1* (referred to hereafter as *Smchd1MD1*), although one of the two X chromosomes undergoes random XCI during early post-implantation development, many genes on the X chromosome thus inactivated become reactivated later on as development progresses, resulting in embryonic lethality at mid-gestation stages (Blewitt et al., 2008). Derepression of X-inactivated

[1]Department of Advanced Bioscience, Graduate School of Agriculture, Kindai University, Nara 631-8505, Japan. [2]Department of Biological Science, Graduate School of Science, Osaka University, Toyonaka 560-0043, Japan. [3]Medical Institute of Bioregulation, Kyushu University, Fukuoka 812-8582, Japan. [4]Agricultural Technology and Innovation Research Institute, Kindai University, Nara 631-8505, Japan.

*Authors for correspondence (nagao@bio.sci.osaka-u.ac.jp; tsado@nara.kindai.ac.jp)

S.I., 0000-0002-8655-4527; K.N., 0000-0003-1418-6988; T. Sakaguchi, 0000-0001-5717-072X; T. Sado, 0000-0002-1232-0250

DEVELOPMENT

1

genes in the homozygous mutant female embryos is accompanied by a reduction in CpG methylation and H3K27me3, suggesting that SmcHD1 is involved in the establishment of the epigenetic state required for the stable maintenance of XCI (Sakakibara et al., 2018). More recent studies have also suggested that SmcHD1 is involved in organization of the higher-order chromatin structure of the Xi (Gdula et al., 2019; Jansz et al., 2018a; Wang et al., 2018), and this is consistent with our previous finding that depletion of SMCHD1 diminishes condensed Barr body conformation in human somatic cells (Nozawa et al., 2013).

Although our previous study demonstrated the role of SmcHD1 in establishment of the epigenetic state, it did not address how the aberrant epigenetic state of the Xi resulting in the derepression of X-inactivated genes was created in the absence of SmcHD1, because the findings were essentially based on observations in $Smchd1^{MD1/MD1}$ mouse embryonic fibroblasts (MEFs) (Sakakibara et al., 2018). In this study, we further explored the chromatin state of the Xi and its silencing status using epiblast stem cells (EpiSCs) established from $Smchd1^{MD1/MD1}$ embryos as a model of the post-implantation epiblast that has just undergone XCI. Many of the derepressed genes on the Xi in SmcHD1-deficient MEFs were repressed with enrichment of H3K27me3 in SmcHD1-deficient EpiSCs. Furthermore, the most prominent feature caused by the lack of SmcHD1 in EpiSCs and MEFs was an extensive loss of H3K9me3 enrichment on the Xi, which apparently disturbed the distribution of H3K27me3. Our findings shed light on the hitherto unexpected role of H3K9me3 in the maintenance of XCI, which has not been extensively studied, especially in the mouse. We discuss the role of SmcHD1 in forming H3K27me3 and H3K9me3 blocks on the Xi and their effects on generating robust heterochromatin.

RESULTS
Derivation of EpiSCs from $Smchd1^{MD1/MD1}$ embryos
Although our previous study suggested that a relatively large fraction of the X-linked genes inactivated early on become derepressed by the mid-gestation stage in the SmcHD1 mutant (Sakakibara et al., 2018), the chromosome-wide kinetics of derepression are not clear. To study the XCI state at the early stages of post-implantation development, we took advantage of EpiSCs (Brons et al., 2007; Tesar et al., 2007) as a model for those cells that have just initiated XCI. EpiSCs have been suggested to resemble post-implantation epiblasts, especially the anterior primitive streak of the epiblast at the late gastrulation-stage, in their cellular and molecular phenotypes (Chen et al., 2016; Kojima et al., 2014).

We established EpiSCs from the epiblasts of embryonic day (E) 6.5 embryos recovered from females doubly heterozygous for a dysfunctional $Xist$ allele, either $Xist^{\Delta A}$ (Hoki et al., 2009) or $Xist^{1lox}$ (Sado et al., 2005), and $Smchd1^{MD1}$ crossed with males heterozygous for $Smchd1^{MD1}$ and carrying an X chromosome derived from JF1 (*Mus musculus molossinus*) (X^{JF1}) (Fig. 1A). Because the dysfunctional $Xist$ allele resided on an X chromosome derived from C57Bl/6J (*Mus musculus domesticus*) ($X^{B6-\Delta A}$ or $X^{B6-1lox}$), XCI in these EpiSCs had been exclusively skewed to X^{JF1}. In addition, the presence of many single nucleotide polymorphisms (SNPs) and insertions/deletions (INDELs) between these subspecies enabled us to carry out allele-resolved analysis of X-linked genes. Each of the established EpiSC lines was genotyped by PCR, and a combination of one wild-type and one homozygous mutant line with respect to the $Smchd1$ allele, either $[X^{B6-\Delta A}X^{JF1}; Smchd1^{+/+}]$ and $[X^{B6-\Delta A}X^{JF1}; Smchd1^{MD1/MD1}]$ or $[X^{B6-1lox}X^{JF1}; Smchd1^{+/+}]$ and $[X^{B6-1lox}X^{JF1}; Smchd1^{MD1/MD1}]$, was used for further analyses. The RNA sequencing (RNA-seq)

experiments described below confirmed that these EpiSCs expressed typical marker genes for EpiSCs (Fig. S1A).

We first examined XCI status in EpiSCs deficient for SmcHD1 by two-color RNA fluorescence *in situ* hybridization (RNA-FISH) for $Xist$ and X-linked $Atrx$ expression. $Atrx$ has been shown to be gradually derepressed during post-implantation development in $Smchd1^{MD1/MD1}$ embryos (Sakakibara et al., 2018). In wild-type EpiSCs, expression of $Atrx$ was detected as a pinpoint signal, which did not overlap with the $Xist$ cloud, in the majority of cells positive for $Xist$ (Fig. 1B,C), indicating that $Xist$ RNA accumulated on the Xi repressed $Atrx$. The situation was essentially the same in $Smchd1^{MD1/MD1}$ EpiSCs, suggesting that $Atrx$ was repressed on the Xi even in the absence of SmcHD1. This contrasted with our previous finding in MEFs prepared from $Smchd1^{MD1/MD1}$ fetuses at E13.5, in which $Atrx$ was derepressed on the Xi coated with $Xist$ RNA in 59% of cells (Sakakibara et al., 2018).

To study allelic expression of some additional X-linked genes in EpiSCs before and after induction of differentiation, we carried out RT-PCR by amplifying a fragment containing a restriction site polymorphism between JF1 and B6 and subsequent restriction digestion of the fragment. As X^{JF1} was exclusively inactivated in the EpiSCs, appearance of the JF1-type restriction fragment indicated failure in silencing of the Xi. As shown in Fig. 1D, all five genes examined were exclusively expressed from the B6 alleles in wild-type EpiSCs not only before but also after differentiation, suggesting stable silencing of genes on the Xi. In contrast, although these genes were repressed in $Smchd1^{MD1/MD1}$ EpiSCs before differentiation, $Pdha1$, $G6pd$ (also known as $G6pdx$) and $Hprt$ were found to be expressed from the JF1 alleles in addition to being expressed from the B6 alleles in EpiSCs after induction of differentiation (Fig. 1D). The derepression of these genes in differentiating mutant EpiSCs was consistent with the phenotype of $Smchd1$-deficient embryos, in which X-linked genes inactivated early on by the accumulation of $Xist$ RNA gradually became derepressed at later stages of development. These results supported the idea that EpiSCs could be used as a model for the early post-implantation-stage epiblast to study the effect of SmcHD1-deficiency at a relatively early phase of XCI.

The majority of genes on the Xi were repressed in $Smchd1^{MD1/MD1}$ EpiSCs
To characterize the X-inactivated state in SmcHD1-deficient EpiSCs in more detail, we performed allele-resolved RNA-seq. We compared Xi-probability of respective X-linked genes (%Xi; percentage of reads derived from the inactive paternal X in total reads derived from both inactive paternal X and active maternal X) between wild-type and $Smchd1^{MD1/MD1}$ EpiSCs. Genes with an Xi-probability of 10% or higher were referred to as those expressed from the Xi (Peeters et al., 2014). The majority of genes in wild-type EpiSCs were scored lower than 10%, indicating that they were essentially inactivated as expected (Fig. 2A). Of 386 informative X-linked genes, 17 (4%) deviated from this category in wild-type EpiSCs, which was comparable to the number in wild-type MEFs (10/448, 2%). They might have not yet been inactivated or might have escaped inactivation in EpiSCs (Table S1). This was also the case in another line of EpiSCs (Fig. S1B,C, Table S1). In contrast to wild-type EpiSCs, 21% (77/369) of the X-linked genes subject to XCI showed an Xi-probability higher than 10% in $Smchd1^{MD1/MD1}$ EpiSCs, and therefore were considered to be misexpressed from the inactive X^{JF1} (Fig. 2A). Although it was reasonable to assume that such misexpression was caused by the lack of SmcHD1, it was not clear whether these genes were derepressed after inactivation at the

2
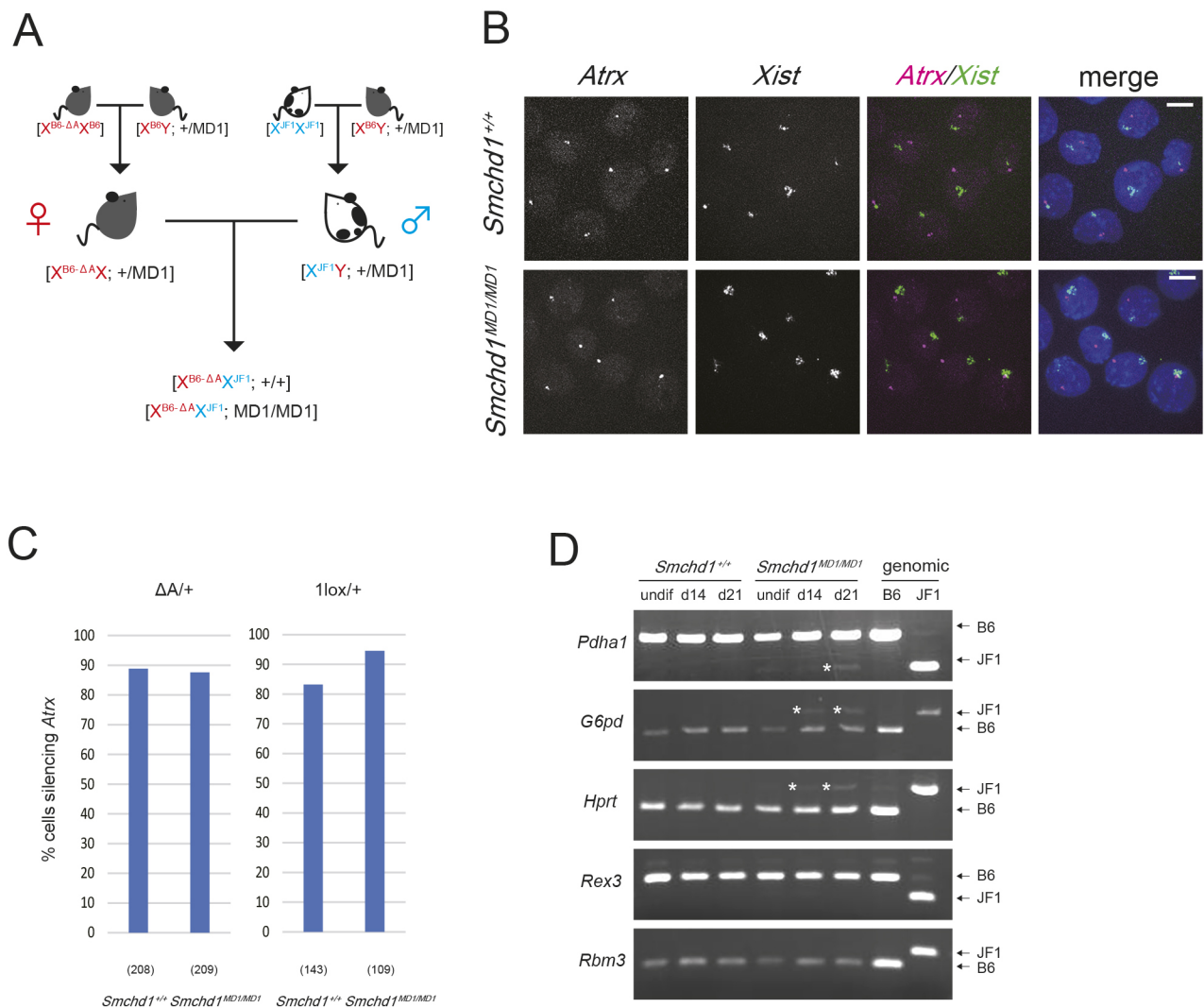
Fig. 1. Expression of the X-linked *Atrx* gene in *Smchd1$^{MD1/MD1}$* EpiSCs. (A) Scheme of mouse intercrosses to obtain post-implantation epiblasts carrying the genotypes from which EpiSCs were derived. (B) Representative images of RNA-FISH detecting *Xist* (green) and *Atrx* (magenta) expression in the nuclei of wild-type and *Smchd1$^{MD1/MD1}$* EpiSCs. Scale bars: 10 μm. (C) Proportions of nuclei with a single pinpoint for *Atrx*, which did not overlap with the *Xist* cloud, in wild-type and *Smchd1$^{MD1/MD1}$* EpiSCs on either *Xist^{ΔA}*/+ or *Xist^{1lox}*/+ background. The numbers of nuclei examined are shown in parentheses. (D) Allelic expression of X-linked genes in EpiSCs before and after induction of differentiation. A fragment containing a restriction site polymorphism amplified by RT-PCR was digested with an appropriate restriction enzyme and electrophoresed. Digestion of a PCR fragment amplified on genomic DNA of B6 and JF1 is also shown in parallel to indicate allelic difference of the restriction fragment. Asterisks highlight a fragment indicative of derepression from the inactive X^{JF1} on the left.

earlier stages, or if instead they failed to be inactivated from the beginning. Nonetheless, they are referred to as derepressed genes hereafter. Although a fraction of genes on the Xi were derepressed in *Smchd1$^{MD1/MD1}$* EpiSCs, cumulative distribution plots showed that changes in X-linked gene expression between wild-type and SmcHD1-deficient EpiSCs were comparable to the autosomal profile, in contrast to the changes in MEFs, indicating that the Xi genes were not substantially upregulated in *Smchd1$^{MD1/MD1}$* EpiSCs (Fig. S1D). Fig. 2B shows the overlap of the derepressed genes in *Smchd1$^{MD1/MD1}$* MEFs and EpiSCs among the 354 informative genes commonly silenced on the Xi in both wild-type EpiSC lines. Of 72 derepressed genes in *Smchd1$^{MD1/MD1}$* EpiSCs, 62 were included in those derepressed in *Smchd1$^{MD1/MD1}$* MEFs. This demonstrated that of 201 derepressed genes in *Smchd1$^{MD1/MD1}$* MEFs, 139 (69%) were repressed on the Xi in *Smchd1$^{MD1/MD1}$* EpiSCs, suggesting that most of the X-linked genes derepressed in mutant MEFs had undergone inactivation in the undifferentiated

epiblast even in the absence of SmcHD1. To evaluate the potential bias of differential gene upregulation depending on developmental stages of cells for these differences, we compared expression levels of these derepressed genes on the active X in female embryonic stem cells (ESCs), EpiSCs, and MEFs in the wild-type background. As shown in Fig. 2C, all but two of the 354 informative genes were expressed in any of ESCs, EpiSCs, and MEFs [fragments per kilobase of exon per million fragments mapped (FPKM)>0], indicating that most of the genes on the Xi had undergone inactivation in EpiSCs. There was a trend of higher expression in MEFs than in EpiSCs for the genes derepressed only in MEFs but not for those derepressed in both, suggesting that differential gene regulation between EpiSCs and MEFs may partly contribute to an increase in the frequency of derepression in MEFs. It is also worth mentioning that genes depressed in *Smchd1$^{MD1/MD1}$* MEFs tended to have relatively high Xi-probability, even though they were classified as inactivated genes (%Xi<10%) in
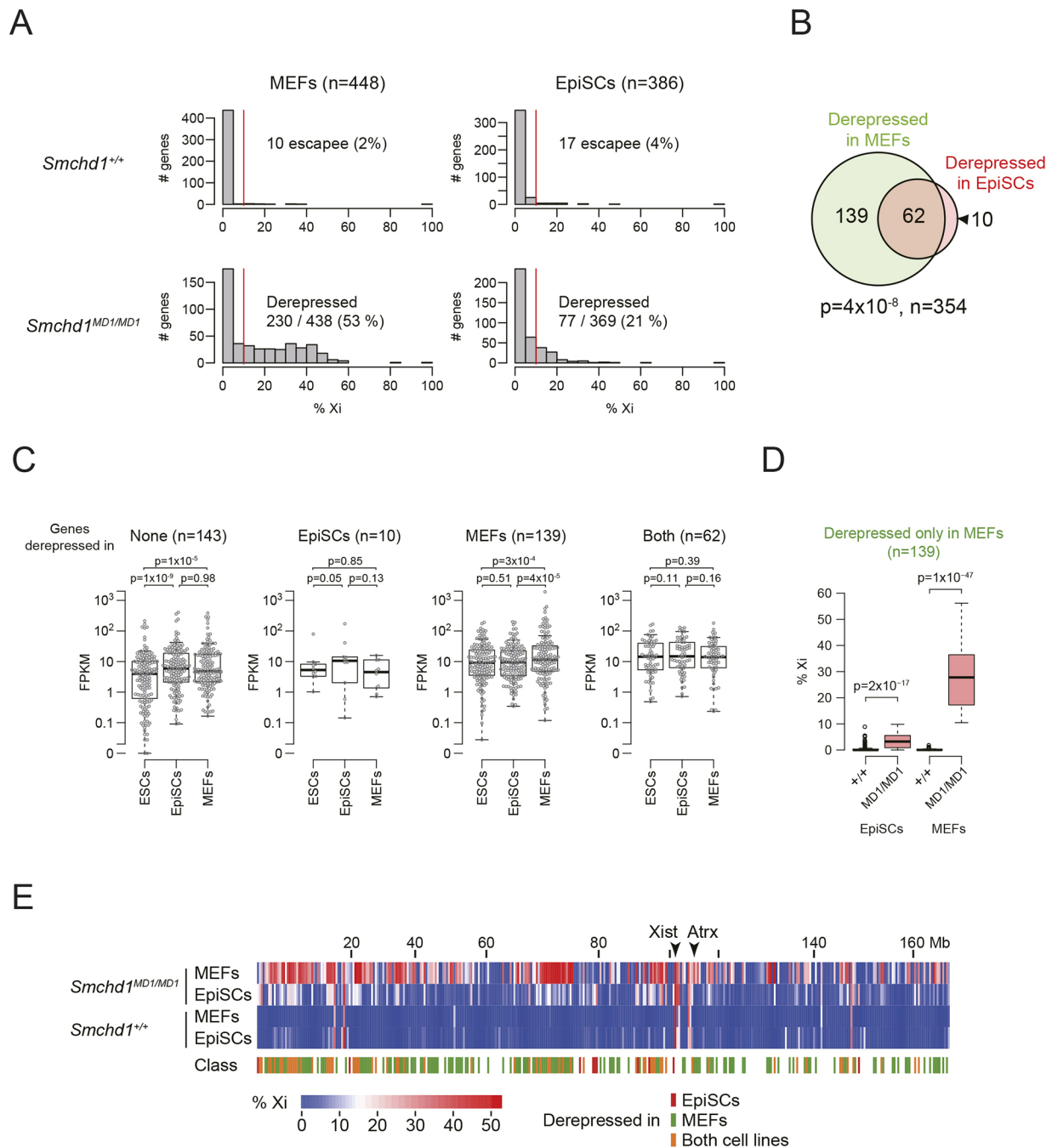
Fig. 2. Chromosome-wide analysis of gene expression on the Xi in *Smchd1*[MD1/MD1] EpiSCs. (A) Histograms showing the numbers of genes with the respective scores of Xi-probability (%Xi) in wild-type (top) and *Smchd1*[MD1/MD1] (bottom) MEFs (left) and EpiSCs (right) on a *Xist*[ΔA]/+ background. Red line indicates the threshold (%Xi=10%) of whether genes were expressed on the Xi. (B) Venn diagram showing the number of genes derepressed in mutant MEFs and EpiSCs among the 354 informative genes commonly silenced in both wild-type EpiSC lines and their overlap. *P*-value, chi-squared test. (C) Box plots showing expression levels (FPKM) of genes depressed in EpiSCs, MEFs, and both on the active X in ESCs, EpiSCs and MEFs in the wild-type background. Note that the expression levels in female ESCs were adjusted to those for a single active X. *P*-value, Wilcoxon test (paired, two-sided). (D) Box plot showing %Xi of 139 genes derepressed only in the mutant MEFs in wild-type and *Smchd1*[MD1/MD1] EpiSCs and MEFs. *P*-value, Wilcoxon test (paired, two-sided). (E) Heatmap showing %Xi of respective informative X-linked genes along the chromosome in wild-type and *Smchd1*[MD1/MD1] MEFs and EpiSCs. Class indicates which category in the Venn diagram shown in B each X-linked gene belongs to, color-matched to the Venn diagram.

Smchd1[MD1/MD1] EpiSCs (Fig. 2D), implying that they were barely repressed. In addition, these genes with relatively higher Xi-probability were distributed across the whole chromosome (Fig. 2E). These findings suggest that the repressive state of the Xi in *Smchd1*[MD1/MD1] EpiSCs was not as robust as that in wild-type EpiSCs.

SmcHD1 has also been suggested to play a role in DNA methylation at a subset of gene loci on the Xi (Gendrel et al., 2012). Gendrel et al. previously reported that CGIs on the Xi can be classified into fast- and slow-methylating CGIs, and they suggest that the kinetics of methylation is regulated by SmcHD1-independent and -dependent pathways, respectively. We wondered

if there was any correlation in the kinetics of CGI methylation when comparing genes derepressed in both EpiSCs and MEFs and those derepressed only in MEFs in the SmcHD1-deficient background. Among the 186 genes in our data set with information of CGI methylation kinetics, genes associated with slow-methylating CGIs were significantly enriched in those depressed in both EpiSCs and MEFs (Fig. S1E).

H3K27me3 and H2AK119ub on the Xi were more intensely stained by immunohistochemistry in *Smchd1$^{MD1/MD1}$* EpiSCs than in wild-type EpiSCs

It has been shown that the Xi in female mouse somatic cells is enriched for repressive histone modifications, such as H3K27me3 and H2AK119ub (Erhardt et al., 2003; Fang et al., 2004; Napoles et al., 2004; Plath et al., 2003; Silva et al., 2003). Although another repressive histone modification, H3K9me3, is also enriched on the

Xi in human and other mammals (Chadwick and Willard, 2004; Chaumeil et al., 2011; Nozawa et al., 2013; Rens et al., 2010; Zakharova et al., 2011), it is known to be undetectable in the mouse by immunofluorescence (Chaumeil et al., 2011; Sado and Sakaguchi, 2013). We first performed immunostaining of wild-type and *Smchd1$^{MD1/MD1}$* EpiSCs using antibodies against H3K27me3 and H2AK119ub. It was evident that both modifications formed one large overlapping accumulation in the nucleus in not only wild-type but also *Smchd1$^{MD1/MD1}$* EpiSCs, suggesting that these modifications were enriched on the Xi in the mutant EpiSCs (Fig. 3A). Because fluorescence for these modifications was rather intense in the mutant EpiSCs, we compared the signal intensity of these modifications between wild-type and mutant EpiSCs. The results demonstrated that immunofluorescence for both H3K27me3 and H2AK119ub was significantly higher in the mutant than in wild-type EpiSCs
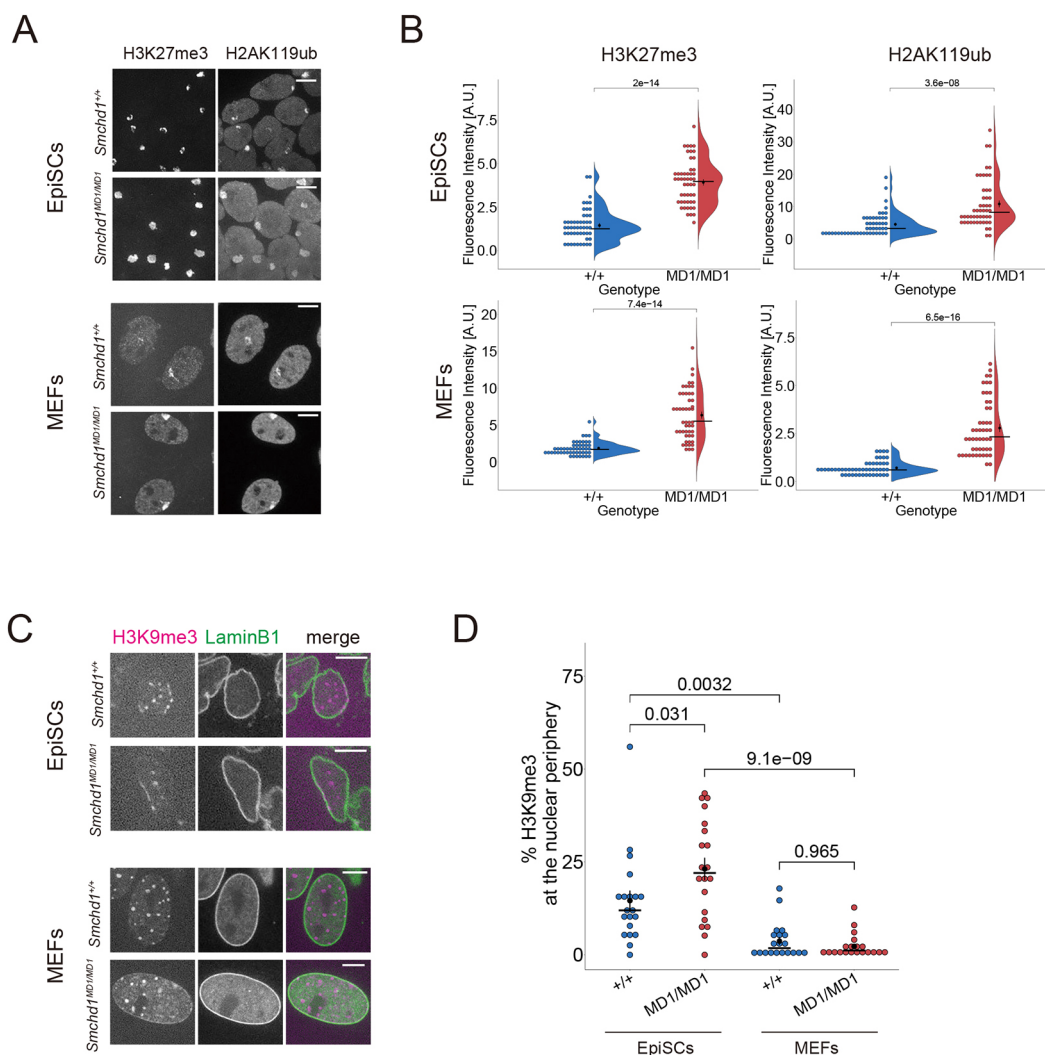
Fig. 3. Histone modifications in wild-type and *Smchd1$^{MD1/MD1}$* EpiSCs and MEFs. (A) Immunofluorescence of wild-type and *Smchd1$^{MD1/MD1}$* EpiSCs and MEFs for H3K27me3 and H2AK119ub. Both modifications were enriched on the inactive X chromosome regardless of the genotype. Scale bars: 10 μm. (B) Signal intensity of the immunofluorescence produced by the antibodies against H3K27me3 and H2AK119ub in 50 nuclei were compared between wild-type (blue) and *Smchd1$^{MD1/MD1}$* (red) EpiSCs (top) and their MEF counterparts (bottom). The black filled circle and horizontal bar indicate mean and median, respectively. Error bar represents s.e.m. *P*-value, Wilcoxon test (unpaired, two-sided). A.U., arbitrary units. (C) Immunofluorescence of wild-type and *Smchd1$^{MD1/MD1}$* EpiSCs and MEFs for H3K9me3 (magenta) in combination with lamin B1 (green). Images are of nuclei in respective cells as indicated on a single plane. Scale bars: 10 μm. (D) Dot plot showing the proportion of H3K9me3 signals at the nuclear periphery marked by lamin B1 relative to those detected in the nucleus in wild-type (blue) and *Smchd1$^{MD1/MD1}$* (red) EpiSCs and MEFs. Twenty nuclei were examined in each cell type. The black filled circle and horizontal bar indicate mean and median, respectively. Error bar represents s.e.m. *P*-value, Tukey-Kramer test.

(Fig. 3B). This was also the case in the comparison between *Smchd1*[MD1/MD1] and wild-type MEFs (Fig. 3A,B) as previously reported (Jansz et al., 2018b). Western blotting, however, demonstrated that global levels of these modifications were comparable between *Smchd1*[MD1/MD1] and wild-type EpiSCs and also between the corresponding MEFs (Fig. S2). Given the effects of SmcHD1 deficiency on gene expression, although the increase in the signal intensity in mutant EpiSCs and MEFs was apparently contradictory, this could be caused by some changes in higher order of the chromatin structure (see Discussion).

We also performed immunostaining for H3K9me3 in combination with H3K27me3. The Xi highlighted with antibody against H3K27me3 in both wild-type and *Smchd1*[MD1/MD1] EpiSCs was barely stained with an antibody against H3K9me3 (Fig. S3A). This was also the case when the Xi was visualized by RNA-FISH detecting *Xist* RNA in combination with immunostaining against H3K9me3 (Fig. S3B). These results demonstrated that, as was the case in MEFs, H3K9me3 was not detectable by immunofluorescence on the Xi in EpiSCs. It was of interest to find, however, that accumulation of H3K9me3 in EpiSCs was distinct in distribution in the nucleus from that in MEFs regardless of SmcHD1 deficiency. Whereas immunofluorescence signals produced in MEFs were discrete and located more interiorly in the nucleus,

forming several distinct chromocenters, they were distributed at the periphery of the nucleus in EpiSCs (Fig. 3C,D). To quantify the spatial differences of H3K9me3 localization in the nucleus between MEFs and EpiSCs, we carried out immunostaining for H3K9me3 in combination with the nuclear lamina marker lamin B1 (Fig. 3C,D). The proportion of H3K9me3 fluorescence overlapping with lamin B1 fluorescence at the nuclear periphery in total fluorescence of H3K9me3 in the nucleus was measured (Fig. S3C). The results demonstrated significant differences in the peripheral distribution of H3K9me3 between EpiSCs and MEFs regardless of the genotype, suggesting that heterochromatin enriched with H3K9me3 in EpiSCs is different in nature from that in differentiated cells such as MEFs.

Lrif1 accumulates on the limited region of the Xi in EpiSCs and its association with heterochromatin is lost in the absence of SmcHD1

It has been suggested that both SmcHD1 and its interacting factor Lrif1, a mouse ortholog of human HBiX1 (LRIF1), accumulate on the Xi and facilitate chromatin condensation in differentiated female cells (Brideau et al., 2015; Nozawa et al., 2013). In female MEFs, antibodies raised against each of these proteins produced an intense signal on the Xi (Fig. 4A,C; Fig. S4). Lrif1 also localized on DAPI-dense heterochromatin forming chromocenters (75.0%, $n=56$),
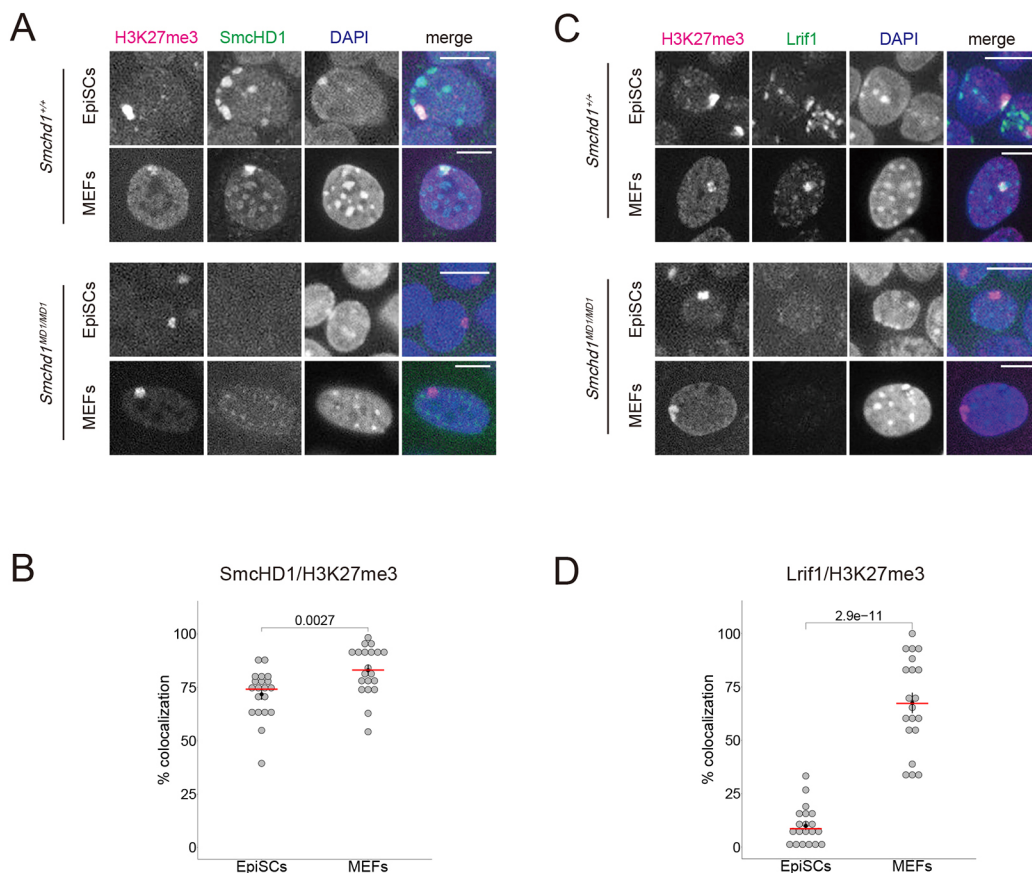
Fig. 4. Cellular localization of SmcHD1 and Lrif1 in wild-type and *Smchd1*[MD1/MD1] EpiSCs and MEFs. (A) Immunofluorescence of wild-type and *Smchd1*[MD1/MD1] EpiSCs for SmcHD1 and H3K27me3 in comparison with that of wild-type and *Smchd1*[MD1/MD1] MEFs. Images are of nuclei on a single plane in respective cells as indicated. Scale bars: 10 μm. (B) Dot plot showing the extent of colocalization between SmcHD1 and H3K27me3 in 20 nuclei of wild-type EpiSCs and MEFs. The black filled circle and horizontal bar indicate mean and median, respectively. Error bar represents s.e.m. (C) Immunofluorescence of wild-type and *Smchd1*[MD1/MD1] EpiSCs for Lrif1 and H3K27me3 in comparison with that of wild-type and *Smchd1*[MD1/MD1] MEFs. Images are of nuclei on a single plane in respective cells as indicated. Scale bars: 10 μm. (D) Dot plot showing the extent of colocalization between Lrif1 and H3K27me3 in 20 nuclei of wild-type EpiSCs and MEFs. The black filled circle and red horizontal bar indicate mean and median, respectively. Error bar represents s.e.m. *P*-value, Wilcoxon test (unpaired, two sided) in B and D.

whereas SmcHD1 was detected on chromocenters in a smaller fraction of cells than Lrif1 (34.7%, *n*=98) in MEFs (Fig. S4). We examined the Xi localization of SmcHD1 and Lrif1 in EpiSCs using the respective antibodies in combination with an anti-H3K27me3 antibody. Although immunofluorescence signals for SmcHD1 largely overlapped with the Xi marked with H3K27me3 in wild-type EpiSCs, as expected (Fig. 4A; Fig. S4), Lrif1 immunofluorescence signals were detected only in a limited part of the H3K27me3 domain representing the Xi (Fig. 4C; Fig. S4). Comparison of Lrif1 occupancy in the H3K27me3 domain revealed significant differences between EpiSCs and MEFs (Fig. 4D). The same quantitative analysis also revealed that SmcHD1 occupancy in the H3K27me3 domain was slightly lower in EpiSCs than in MEFs (Fig. 4B). Furthermore, it was of interest to find that Lrif1 lost its specific localization in the nuclei of both EpiSCs and MEFs homozygous for *Smchd1^{MD1}* (Fig. 4C; Fig. S4B). This was not due to downregulation of Lrif1, as similar levels of the protein were detected in wild-type and *Smchd1^{MD1/MD1}* EpiSCs and MEFs by western blotting (Fig. S5), suggesting that the localization of Lrif1 depends on SmcHD1. Lrif1, however, localizes at only a limited region of the Xi despite the presence of SmcHD1 on the Xi in wild-type EpiSCs. Although the reason for this was unknown, the differential occupancy of Lrif1 and SmcHD1 on the Xi between EpiSCs and MEFs suggested the differences in the chromatin state of their Xi.

SmcHD1-dependent X-linked genes with lower enrichment of H3K27me3 in mutant MEFs have acquired H3K27me3 in EpiSCs

We previously demonstrated that X-linked genes that are derepressed in MEFs prepared from E13.5 *Smchd1^{MD1/MD1}* fetuses showed a lower enrichment of H3K27me3 and belong to a group of genes with relatively lower enrichment of H3K27me3 at the blastocyst stage of wild-type embryos (Sakakibara et al., 2018). This finding suggests that in *Smchd1^{MD1/MD1}* embryos, these X-linked genes fail to acquire H3K27me3 or to maintain H3K27me3 acquired early on during post-implantation development owing to the absence of SmcHD1 and eventually become derepressed. To explore these possibilities, we examined the H3K27me3 state in *Smchd1^{MD1/MD1}* EpiSCs. Chromatin immunoprecipitation (ChIP) using an antibody against H3K27me3, and subsequent quantitative PCR (qPCR) were carried out to see the enrichment of sequences at two X-linked loci, *Hprt* and *Rlim*, which were derepressed in *Smchd1^{MD1/MD1}* MEFs but repressed in *Smchd1^{MD1/MD1}* EpiSCs. The relative enrichment of H3K27me3 at these loci in *Smchd1^{MD1/MD1}* EpiSCs was comparable to or even slightly higher than that in wild type (Fig. 5). When the same ChIP-qPCR was performed using chromatin prepared from *Smchd1^{MD1/MD1}* MEFs, lower enrichment of H3K27me3 was evident in *Smchd1^{MD1/MD1}* MEFs than in wild-type MEFs, consistent with our previous ChIP-seq result (Sakakibara et al., 2018). This finding suggests the possibility that these two X-linked genes acquire H3K27me3 during early post-implantation development but fail to maintain it and become derepressed thereafter in the absence of SmcHD1.

SmcHD1 deficiency results in substantial loss of H3K9me3 enrichment on the Xi in EpiSCs

Subsequently, the chromosomal distribution of H3K27me3 and H3K9me3 was examined by allele-resolved ChIP-seq. H3K27me3 was virtually absent on the Xa but was distributed along the Xi to form blocks in both wild-type EpiSCs and MEFs, as expected (Fig. 6A; Fig. S6A). In addition, the Xi showed clear enrichment of
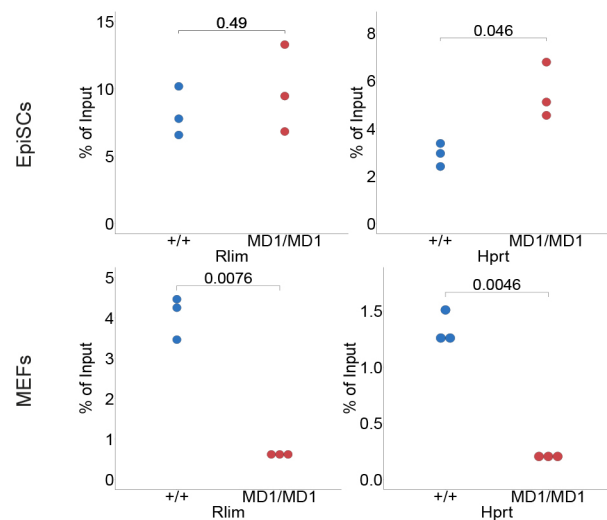
Fig. 5. H3K27me3 states at X-inactivated gene loci in wild-type and *Smchd1^{MD1/MD1}* EpiSCs. ChIP against H3K27me3 and subsequent qPCR analysis at the *Rlim* and *Hprt* loci in wild-type (blue) and *Smchd1^{MD1/MD1}* (red) EpiSCs in comparison with that in the respective MEFs. *P*-value, Welch's *t*-test.

H3K9me3 as blocks in wild-type MEFs, in agreement with a previous report by Keniry et al. (2016), and the same was true in wild-type EpiSCs (Fig. 6A) even though immunostaining did not show obvious localization of H3K9me3 on the Xi in either case. In EpiSCs homozygous for *Smchd1^{MD1}*, the distribution of H3K27me3 on the Xi was, at a glance, similar to that in wild type, but, in fact, expanded its occupancy to some extent as shown in the overlay track in Fig. 6A. This trend was more pronounced in MEFs. Most interestingly, the enrichment of H3K9me3 was greatly diminished and became restricted only to limited regions on the Xi in the mutant EpiSCs. We quantified the occupancy of H3K9me3 and H3K27me3 along the Xi in wild-type and *Smchd1^{MD1/MD1}* EpiSCs and the respective counterpart of MEFs (Fig. 6B,C; Fig. S7A). Fig. 6B shows that in wild-type EpiSCs, 26.7% and 17.4% of the regions on the Xi were enriched solely with H3K9me3 and H3K27me3, respectively, and the remaining majority of 55.6% regions harbored both. In *Smchd1^{MD1/MD1}* EpiSCs, however, H3K27me3 not only replaced the one-third of the regions enriched solely with H3K9me3 in wild-type EpiSCs but also spread into the remaining two-thirds. In addition, the majority of H3K27me3- and H3K9me3-overlapping regions in wild-type EpiSCs (55.6%) lost the distribution of H3K9me3 and became enriched solely with H3K27me3 in *Smchd1^{MD1/MD1}* EpiSCs. Scatter plots in Fig. 6C displaying pairwise comparison of H3K27me3 and H3K9me3 enrichment within 50-kb windows across the Xi between wild-type and *Smchd1^{MD1/MD1}* cells also clearly demonstrate that although enrichment of H3K27me3 increased, H3K9me3 was extensively diminished on the Xi in *Smchd1^{MD1/MD1}* EpiSCs. These situations were essentially the same in the mutant MEFs as well. The coverage of the respective histone modifications on the Xa and autosomes as well as that on the Xi was compared between EpiSCs and MEFs (Fig. S7A). The coverage of H3K9me3 on the Xi was reduced by one-quarter and one-half of wild-type in mutant EpiSCs and MEFs, respectively, and a slight but discernible reduction was also observed on the Xa and autosomes in MEFs. The coverage of H3K27me3, by contrast, increased only on the Xi in mutant cells of both cell types. Although loss of H3K9me3 was less extensive in MEFs compared with EpiSCs, it still accompanied gains and expansions of H3K27me3 on
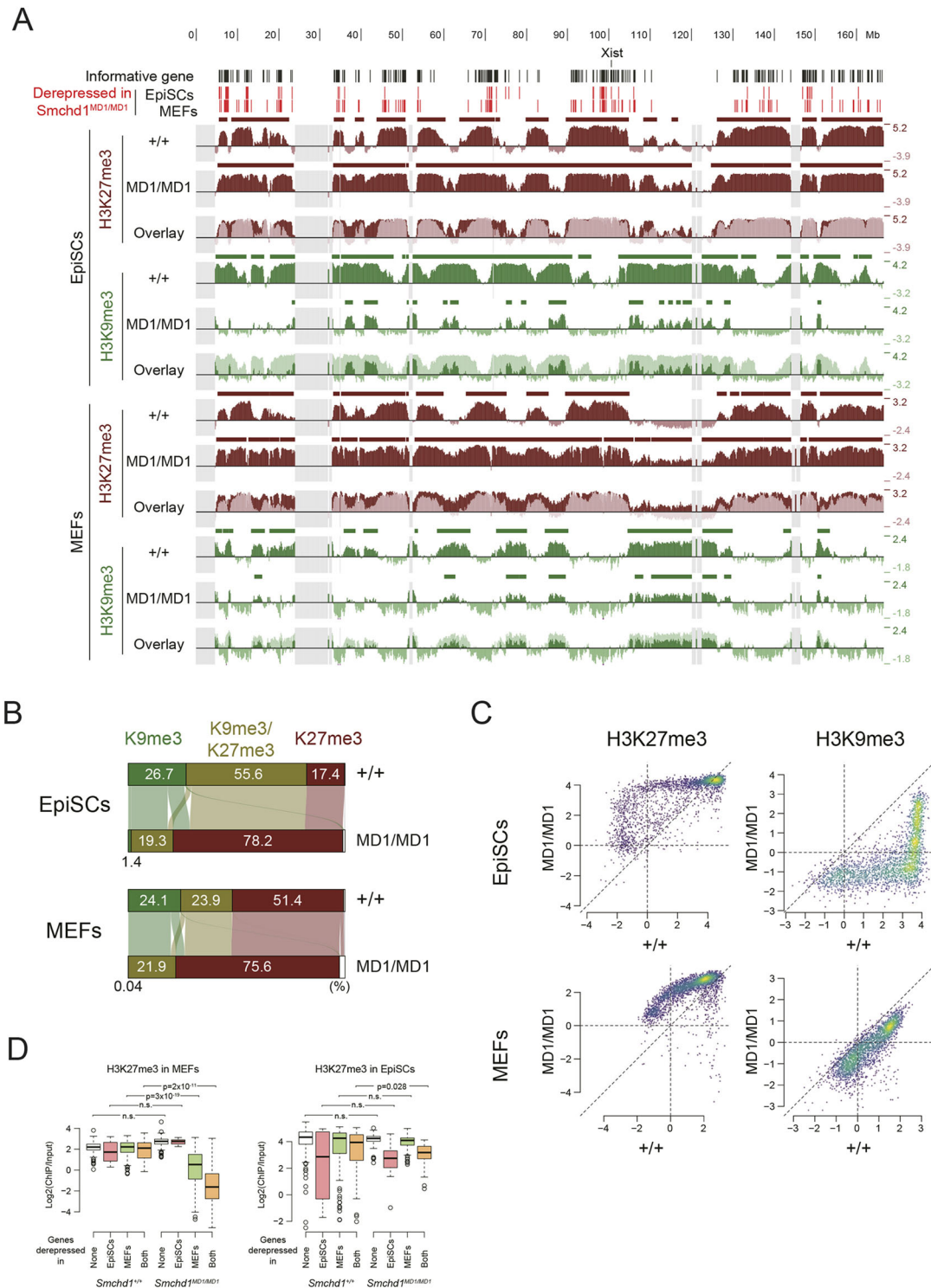
Fig. 6. Histone modification states revealed by ChIP-seq in wild-type and *Smchd1^MD1/MD1* EpiSCs and MEFs. (A) Distribution of H3K9me3 and H3K27me3 on the Xi in wild-type and *Smchd1^MD1/MD1* EpiSCs in comparison with that in the respective MEFs revealed by ChIP-seq. Enrichments or depletions of the respective histone modifications over or below the genome-wide average of wild-type MEFs, respectively, are shown as log2(ChIP/Input) per non-overlapping 150-kb bin in parallel with the locations of derepressed genes. Horizontal bars shown on the top of the respective tracks represent the EDD domains indicating the span of how far the enrichments over the genome-wide average are consecutively spread along the chromosome. An overlay is also shown to visualize the difference in the distribution of the respective modifications in wild-type (pale color) and *Smchd1^MD1/MD1* (deep color) cells. Unmappable regions are indicated by gray. (B) Alluvial diagrams showing differences in the occupancies of either H3K9me3 or H3K27me3 alone or both on the Xi between wild-type and *Smchd1^MD1/MD1* cells of EpiSCs (top) and MEFs (bottom) using the EDD domains shown in A. (C) Scatter plots showing pairwise comparison of H3K27me3 (left) and H3K9me3 (right) enrichment within 50-kb windows across the Xi between wild-type and *Smchd1^MD1/MD1* cells of EpiSCs (top) and MEFs (bottom). (D) Box plot showing H3K27me3 enrichment within gene bodies for each group of genes classified in Fig. 2B according to the state of derepression (MEF specific, EpiSC specific, both, and not derepressed) in MEFs and EpiSCs. The color of each box matches the color of each group in the Venn diagram shown in Fig. 2B. *P*-value, Wilcoxon test (paired, one-sided). n.s, not significant (*P*>0.05).

the Xi (Fig. 6B,C; Fig. S7A). These analyses demonstrated that loss of SmcHD1 diminished the occupancy of H3K9me3 and facilitated the replacement with or expansion of H3K27me3 on the Xi in *Smchd1*$^{MD1/MD1}$ EpiSCs and MEFs. In addition, the regions that still retained some enrichment of H3K9me3 on the Xi in the mutant EpiSCs included those showing slight enrichment of H3K9me3 on the Xa (Fig. S6B). Interestingly, the Xi and Xa in MEFs exhibited mutually similar distribution of H3K9me3 regardless of the presence or absence of SmcHD1, although the extent of H3K9me3 enrichment was lower in the SmcHD1-deficient background. Given that the enrichment and expansion of H3K9me3 was observed even on the Xa in the wild-type background when compared between EpiSCs and MEFs, formation of H3K9me3 blocks could have a structural impact on the X chromosome. The H3K9me3-enriched regions on the Xa in EpiSCs could serve as the primary sites for H3K9me3 deposition on both the Xa and Xi, from which H3K9me3 spreads to form large blocks on the Xi. The observation that the H3K9me3 blocks, although they were attenuated, were formed on the Xi in *Smchd1*$^{MD1/MD1}$ MEFs suggested that deposition and spreading of H3K9me3 were not necessarily compromised in the absence of SmcHD1. It is worth mentioning that the reduction in the enrichment of H3K9me3 was not only confined to the Xi but also observed at autosomal regions in both SmcHD1-deficient EpiSCs and MEFs, although it was less pronounced than the reduction on the Xi (Fig. 6C; Fig. S7B,C). These results demonstrate that the most prominent effects caused by a functional loss of SmcHD1 in the mutant cells is substantial loss of H3K9me3 on the Xi.

Effects of SmcHD1 deficiency on H3K27me3 on the Xi

To gain more insight into the kinetics of H3K27me3 on the Xi, the enrichment of H3K27me3 at the derepressed loci in mutant MEFs was compared between MEFs and EpiSCs. Fig. S7D shows the distribution of H3K27me3 and H3K9me3 at representative loci among different categories of genes on the Xi in EpiSCs and MEFs. *Rlim* and *Atrx* in mutant EpiSCs, although they are derepressed with lower enrichment of H3K27me3 in the mutant MEFs, were silenced on the Xi (%Xi<10%) with higher enrichment of H3K27me3. Whereas genes that were derepressed in both mutant EpiSCs and MEFs, such as *Ogt*, manifested lower enrichment of H3K27me3, those stably repressed in both, such as *Fndc3c1*, displayed higher enrichment of H3K27me3. Lower enrichment of H3K27me3 was evident at the loci of *Xist* as well as 'escapees' (genes that escape X inactivation) on the Xi in both wild-type and mutant EpiSCs and their counterpart of MEFs. However, whether genes were embedded in H3K9me3-enriched regions or not was not necessarily correlated with the transcriptional status of genes on the Xi, such as *Atrx* and *Rlim* in EpiSCs and *Fndc3c1* between EpiSCs and MEFs. The box plots in Fig. 6D show that in the SmcHD1-deficinet background, a group of genes that were derepressed only in MEFs (represented by green in Figs 2B and 6D) manifested high enrichment of H3K27me3 in EpiSCs but not in MEFs, and this enrichment was comparable with those genes that stayed repressed in both EpiSCs and MEFs (the group of genes in white in Fig. 6D). We assume that these derepressed genes in mutant MEFs are likely to be a class of genes that lose H3K27me3 at later developmental stages, which has been deposited for silencing during the early phase of XCI, in SmcHD1-deficient embryos and suggest that their Xi is defective in establishing the chromatin state that enables sustaining H3K27me3. There was no significant correlation between the extent of H3K9me3 enrichment and gene derepression (Fig. S7E).

DISCUSSION

Although our previous study suggested that SmcHD1 is involved in establishment of epigenetic states required for stable silencing of X-inactivated genes, it remained unaddressed how the lack of SmcHD1 affects the dynamics of histone modifications during development. To understand the mechanism by which SmcHD1 contributes to establishing the epigenetic state of the Xi, we took advantage of EpiSCs derived from the undifferentiated post-implantation epiblast, in which XCI has already been initiated but is thought to be midway to the fully established state seen in MEFs. Differences in the localization of Lrif1 on the Xi and the nuclear distribution of H3K9me3 between EpiSCs and MEFs would support the idea that chromatin in EpiSCs is in a transitional state.

Allele-resolved RNA-seq of wild-type and *Smchd1*$^{MD1/MD1}$ EpiSCs revealed that the majority of informative genes on the Xi were classified as being repressed and only about 20% of them were misexpressed on the Xi in *Smchd1*$^{MD1/MD1}$ EpiSCs, indicating that genes on the Xi are substantially silenced in *Smchd1*$^{MD1/MD1}$ EpiSCs. This contrasts with the fact that more than half of the informative genes on the Xi were derepressed in *Smchd1*$^{MD1/MD1}$ MEFs. In addition, although those silenced in EpiSCs manifested enrichment of H3K27me3, a subset of them were derepressed with lower enrichment of H3K27me3 than the genome-wide average in *Smchd1*$^{MD1/MD1}$ MEFs. These findings suggest the possibility that during development of *Smchd1*$^{MD1/MD1}$ embryos, genes on the X chromosome coated with *Xist* RNA undergo inactivation and acquire H3K27me3 in the epiblast cells, as observed in differentiating wild-type female ESCs (Colognori et al., 2020), but sporadically lose H3K27me3 and become derepressed. Given the previous findings that the Xi is stably silenced in the epiblast lineage of the EED-deficient embryo (Kalantry and Magnuson, 2006), however, it is likely that loss of H3K27me3 alone would not be a reason for depression of X-inactivated genes in mutant cells. DNA hypomethylation at CpG islands is also not sufficient to account for depression of X-inactivated genes in SmcHD1-deficient embryos (Gendrel et al., 2013). Although it is currently unknown how SmcHD1 deficiency affects enrichment of H2AK119ub on the Xi in EpiSCs and MEFs, it is possible that multiple repressive marks, including H2AK119ub, are diminished in SmcHD1-deficient MEFs, rendering the Xi state less stable.

An obvious anomaly found in the chromatin of the Xi in SmcHD1-deficient cells in comparison with wild type was extensive loss of H3K9me3. It should be noted, however, that H3K9me3 still showed some enrichment at limited regions on the Xi over the Xa in mutant EpiSCs and some of H3K9me3 blocks, although they are attenuated, had been formed in the mutant MEFs. It seems, therefore, possible that defects in SmcHD1-deficient cells are neither the deposition of H3K9me3 on the Xi nor the ability to propagate H3K9me3 from such initially deposited sites but rather the extent of enrichment or sufficient spreading of H3K9me3. Nonetheless, it is unlikely that loss of H3K9me3 is directly involved in derepression of X-inactivated genes as whether or not genes are enriched with H3K9me3 does not necessarily correlate with gene activity in wild-type EpiSCs and MEFs. Several lines of evidence using ESCs carrying an inducible *Xist* allele suggest that *Xist*-mediated silencing is triggered by deacetylation of H3K27ac at enhancers and promoters several hours after *Xist* induction and followed by deposition of PRC1-mediated H2AK119ub and subsequently by PRC2-mediated deposition of H3K27me3 on the Xi (Nesterova et al., 2019; Żylicz et al., 2019). In addition, the Xi in differentiating female ESCs has been shown to form essentially the same distributions of H2AK119ub and H3K27me3 on the Xi by day
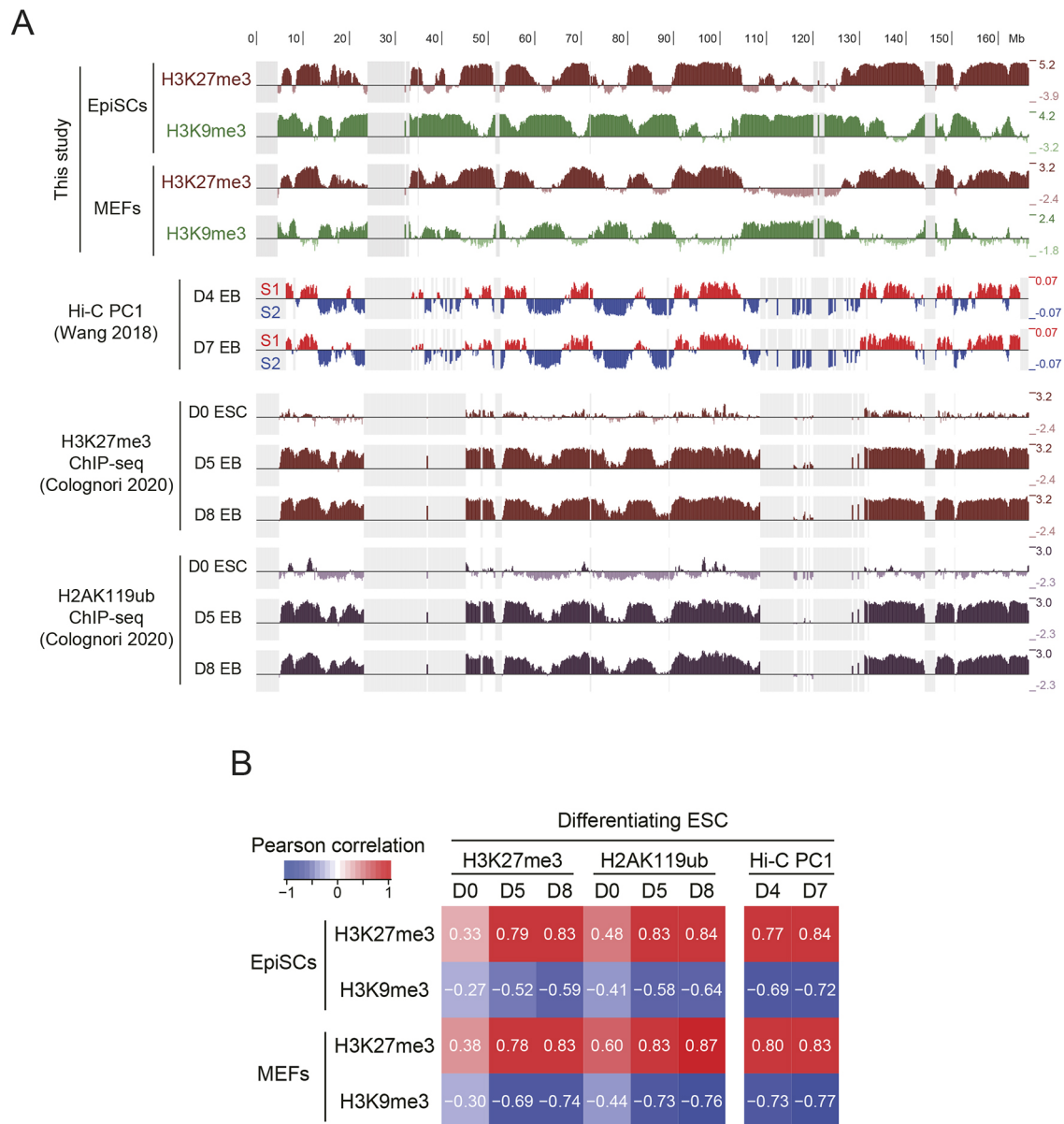
Fig. 7. H3K9me3 blocks on the Xi correlate with S2 compartments. (A) Chromosomal distributions of H3K27me3 and H3K9me3 on the Xi in EpiSCs and MEFs revealed by this study are shown in comparison with those of H3K27me3 and H2AK119ub on the future Xi in ESCs and on the Xi in EBs revealed by Colognori et al. (2020) and those of S1/S2 compartments emerging as PC1 on the Xi in EBs by Hi-C analysis (Wang et al., 2018). (B) Pearson correlation between either H3K27me3 or H3K9me3 enrichments in EpiSCs/MEFs and either H3K27me3 or H2AK119ub enrichments in differentiating ESCs as EBs by Wang et al. (2018) per 50 kb bin were evaluated. Similarly, correlation with Hi-C PC1 values was also evaluated.

5 of differentiation and maintains such distributions thereafter (Colognori et al., 2020), which are highly correlated with the distribution of H3K27me3 in wild-type EpiSCs and MEFs (Fig. 7A). It has also been shown that it is not until around day 7 that SmcHD1 starts to be localized to the Xi during differentiation of female ESCs (Gendrel et al., 2012; Sakata et al., 2017), and the recruitment of SmcHD1 to the Xi is dependent on H2AK119ub in female MEFs (Jansz et al., 2018b). Taking these previous findings all together, we suggest that SmcHD1 recruited to and accumulated on the Xi via H2AK119ub by then plays a crucial role in generating proper H3K9me3 blocks on the Xi and facilitating the establishment of the respective heterochromatin blocks of H3K27me3 and H3K9me3 on the Xi in the epiblast cells prior to differentiation. It seems that forming H3K9me3 blocks on the Xi restricts the eventual occupancy of H3K27me3 and perhaps H2AK119ub, and its failure disturbs the overall distribution of H3K27me3, resulting in irregular expansion of the H3K27me3 blocks, as seen in $Smchd1^{MD1/MD1}$ EpiSCs and MEFs. Propagation of H3K9me3 and subsequently formed blocks of H3K9me3 may facilitate further condensation of the Xi resulting in very robust heterochromatin. In the absence of H3K9me3, the Xi could stay relatively less condensed, allowing access to demethylases of H3K27me3 at particular loci that have been silenced and their eventual derepression. Signal intensity of H3K27me3 and H2AK119ub on the Xi was significantly enhanced in SmcHD1-deficient EpiSCs and MEFs. It is possible that the less-condensed chromatin state of the Xi in the mutant might give the respective antibodies easier access to their target, contributing to an increase in signal intensity.

DEVELOPMENT

A role of SmcHD1 in the regulation of higher-order chromatin structure has been suggested (Gdula et al., 2019; Jansz et al., 2018a; Wang et al., 2018). Wang et al. (2018) proposed that S1/S2 compartments identified by principal component analysis (PCA) of Hi-C data on the Xi in differentiating female ESCs are different from A/B compartments identified by PCA on the Xa and represent an intermediate Xi structure, and that SmcHD1 subsequently folds this structure into a compartment-less Xi super-structure consisting of two large mega-domains, based on the finding that the Xi in SmcHD1-deficient neural precursor cells lacks such mega-domains and harbors the similar S1/S2 compartment-structure instead (Wang et al., 2018). It has been shown that S1 compartments highly correlate with H3K27me3 and H2AK119ub on the Xi in not only embryoid bodies (EBs) differentiated from ESCs but also SmcHD1-deficient neural progenitor cells (NPCs) and immortalized MEFs, and PRC1 partitions the Xi into S1/S2 compartments (Gdula et al., 2019; Wang et al., 2018, 2019). The H3K27me3 and H3K9me3 blocks we detected on the Xi in wild-type EpiSCs and MEFs in this study are highly correlated with S1 and S2 compartments, respectively, emerging on the Xi in wild-type EBs (Fig. 7A,B; Fig. S8). It is, therefore, possible that intra-chromosomal interactions between the regions enriched with either H3K27me3 or H3K9me3 are involved in the emergence of S1 and S2 compartments as PC1 in PCA. Given the findings by Wang et al. (2018) using SmcHD1-deficient NPCs, it would be reasonable to assume that the Xi in our mutant EpiSCs and MEFs fails to form the Xi-specific mega-domains and remains compartmentalized. It is, however, currently unknown whether expansion of H3K27me3 and loss of H3K9me3 affect the distributions of S1/S2 compartments on the Xi in our SmcHD1-deficient EpiSCs and MEFs; therefore, in future studies Hi-C analysis using $Smchd1^{MD1/MD1}$ EpiSCs and MEFs would provide further insights into our understanding of how H3K9me3 participates in S1/S2 compartmentalization and higher-order chromatin structure of the X chromosome. The impact of H3K9me3 on the higher-order chromatin structure of the Xi could also be evaluated by studying enrichment of H3K9me3 on the Xi in EBs derived from wild-type and SmcHD1-deficient ESCs.

As far as we are aware, there has been no direct evidence showing an interaction between SmcHD1 and machinery regulating H3K9me3. A possible link between SmcHD1 and H3K9me3, however, might be envisioned based on previous findings, including ours, that SmcHD1 could associate with heterochromatin protein 1 (HP1), a protein that recognizes and binds H3K9me3, via an interaction with Lrif1 (Brideau et al., 2015; Nozawa et al., 2013). SmcHD1 and Lrif1 localize at heterochromatin enriched with H3K9me3 in EpiSCs. Interestingly, Lrif1 lost its association with DAPI-dense heterochromatin in the absence of SmcHD1 in both EpiSCs and MEFs, suggesting that the localization of Lrif1 at DAPI-dense heterochromatin depends on SmcHD1. It is therefore reasonable to assume that SmcHD1 may have an alternative way to associate with DAPI-dense heterochromatin enriched for H3K9me3 without the interaction with HP1 via Lrif1. Candidates for the factors that associate with SmcHD1 and regulate H3K9me3 on the Xi may be found among factors known to participate in the regulation of H3K9me3 at DAPI-dense heterochromatin.

MATERIALS AND METHODS
Mice
Details of MommeD1 mice have been described elsewhere (Blewitt et al., 2008) and the genetic background of the MommeD1 colony has been replaced essentially by C57Bl/6 (B6) (Leong et al., 2013). Two types of *Xist*

mutants carrying either $Xist^{\Delta A}$ or $Xist^{1lox}$ were described previously (Hoki et al., 2009; Sado et al., 2005) and their genetic background has also been replaced essentially by B6. All of these mice were maintained by crossing heterozygous females with B6 males. Male mice heterozygous for $Smchd1^{MD1}$ with the X chromosome derived from the JF1 strain (X^{JF1}) [$X^{JF1}Y$; $Smchd1^{+/MD1}$] were generated by crossing JF1 females with $Smchd1^{+/MD1}$ males. Females doubly heterozygous for $Smchd1^{MD1}$ as well as one of either $Xist^{\Delta A}$ or $Xist^{1lox}$ were generated by crosses between females with one of the *Xist* mutations and males heterozygous for $Smchd1^{MD1}$. These males and females were crossed to obtain [$X^{B6-\Delta A}X^{JF1}$; $Smchd1^{MD1/MD1}$] or [$X^{B6-1lox}X^{JF1}$; $Smchd1^{MD1/MD1}$] embryos for derivation of EpiSCs and for preparation of MEFs. Primer sequences used for genotyping are shown in Table S2. All mice were maintained and used in accordance with the Guidelines for the Care and Use of Laboratory Animals of Kindai University (KAAG-2020-009).

Cell culture
EpiSCs were established from E6.5 epiblasts in the presence of the Wnt inhibitor IWP-2 according to the previous report by Sugimoto et al. (2015). For passage, cells were treated with 10 µM Y-27632 for 1 h prior to dissociation with Accutase. Dissociated cells were seeded on a layer of feeder cells in the presence of 10 µM Y-27632, and the medium was exchanged daily. MEFs were prepared from fetuses obtained at E13.5 as described previously (Sakakibara et al., 2018).

Differentiation of EpiSCs was carried out as described by Sugimoto et al. (2015). Briefly, clumps of EpiSCs were cultured on a bacteriological Petri dish and allowed to form EBs for 7 days. EBs thus formed were plated on a gelatinized tissue culture dish and cultured for an additional 7 or 14 days to achieve outgrowth of differentiated cells.

RNA-FISH
Plasmid pXist_SS12.9 containing a 12.9-kb *Xist* cDNA fragment (Sakata et al., 2017) and BAC clone RP23-260I15 containing the *Atrx* gene were labeled with Green dUTP and Cy3 dUTP, respectively, by nick translation. EpiSCs or MEFs grown on a coverslip were fixed with 4% paraformaldehyde (PFA) for 10 min. Following permeabilization, blocking in 0.05% Triton X-100/0.05% bovine serum albumin (BSA)/PBS for 30 min, and subsequent dehydration in 70% and 100% ethanol, air-dried specimens were subjected to hybridization as described by Sakata et al. (2017). Cytological preparations using Carnoy's fixative were also made and subjected to hybridization.

Allelic expression analysis by RT-PCR
Total RNA was converted into cDNA using SuperScript III (Invitrogen) using random hexamer as a primer. RT-PCR was subsequently carried out to amplify the fragments containing restriction site polymorphisms using the primer sets in Table S2. PCR products were digested with an appropriate restriction enzyme [*Pdha1*, TaqI; *G6pd*, DraI; *Hprt*, HinfI; *Rex3* (*Bex1*), BsrGI; *Rbm3*, DdeI].

Immuno-RNA-FISH
Cells grown on a coverslip were fixed with 2% PFA/0.5% Triton X-100 for 10 min and subjected to permeabilization and blocking in 0.5% Triton X-100/0.5% BSA/PBS for 30 min. Immunoreaction was carried out using an antibody against H3K9me3 (MABI0318, 305-34833, WAKO, 1:100) in the presence of RNase Out (Invitrogen) at 1 U/µl at 4°C overnight, and subsequently the primary antibody was visualized with CF594-labeled goat anti-mouse IgG antibody (20111, Biotium, 1:1000). Following post-fixation with 4% PFA, RNA-FISH was carried out as described above, with omission of the dehydration process.

Immunofluorescence
Cells were grown on a coverslip. Fixation and subsequent permeabilization and blocking were carried out in a slightly different way depending on the antibody used. For staining of SmcHD1, cells fixed with 0.4% PFA for 7 min were permeabilized with 0.5% Triton X-100/PBS for 10 min, followed by blocking with Blocking One (Nacalai Tesque) for 20 min. The

antibody against SmcHD1 was diluted with Signal Enhancer HIKARI A (Nacalai Tesque). For staining of Lrif1, cells fixed with 0.4% PFA for 10 min were permeabilized and blocked with 0.5% BSA/0.5% Triton X-100/PBS for 30 min. For staining of H3K27me3, H3K9me3, H2AK119ub and lamin B1, cells were fixed in 4% PFA for 10 min, were permeabilized and blocked in 0.5% BSA/0.5% Triton X-100/PBS for 30 min. All antibodies were diluted with 0.05% Tween20/PBS except for co-staining with the antibody against SmcHD1. For co-staining of SmcHD1 and H3K27me3, both antibodies were diluted with Signal Enhancer HIKARI A. Immunoreaction with primary antibodies was carried out overnight at 4°C. Following three washes with 0.05% Tween20/PBS for 5 min, the respective antibodies were visualized by either CF594 goat anti-mouse IgG (Biotium, 1:1000) or CF488A goat anti-rabbit IgG (200015, Biotium, 1:1000). Fluorescence images were taken with an inverted microscope (IX71, Olympus) equipped with an Olympus Disk Scanning Unit (DSU) and an EM-CCD camera (iXon, Andor), and analyzed with MetaMorph imaging software (Molecular Devices).

The antibody against Lrif1 was raised by immunizing rabbits with a His-tagged recombinant protein containing the last 237 amino acids of Lrif1 and affinity-purified using the antigen. The specificity of the antibody was confirmed using EpiSCs established from a Lrif1 knockout embryo (Fig. S5). Antibodies used for this study are listed in Table S3.

Quantification of fluorescence intensity

Signal intensity was analyzed using ImageJ (1.52h). All images examined for signal intensity were acquired under the same conditions. Fluorescence of the Xi visualized as a large domain in the nucleus by antibodies against either H3K27me3 or H2AK119ub was quantified and normalized as follows: (area of a selected domain produced by either antibody×mean fluorescence intensity of selected domain)−(area of the selected domain×mean fluorescence intensity of the nucleoplasm surrounding the selected domain).

The extent of colocalization between signals visualized by two different antibodies was quantified using MetaMorph v7. The threshold of fluorescence produced by each of the two antibodies was manually set on the same single plane of an immunofluorescence image (see Fig. S3C) and the extent of colocalization of the signal produced by each antibody, that is, H3K27me3 and Lrif1, H3K27me3 and SmcHD1, or lamin B1 and H3K9me3, was measured. For colocalization of H3K27me3 and Lrif1 or H3K27me3 and SmcHD1, nuclei to be analyzed were randomly selected among those with a discrete H3K27me3 domain. For colocalization of H3K9me3 and lamin B1, nuclei were randomly selected from those showing clear localization of lamin B1 at the nuclear periphery. Wilcoxon–Mann–Whitney test and Tukey test were conducted using R (4.0.1).

Allele-resolved RNA-seq

EpiSCs grown on feeder cells were treated with Y-27632 and dissociated into single cells using Accutase. The cell suspension was transferred onto a gelatin-coated culture dish and incubated for 30 min at 37°C to remove feeder cells based on their differential adherence. Following one more round of removal of the feeder cells, EpiSCs were collected by centrifugation (270 g for 3 min at room temperature) and disrupted in TRIzol (Ambion). Total RNA was prepared according to the manufacturer's instructions. Libraries were prepared using the TruSeq Stranded mRNA LT Sample Prep Kit (Illumina). Paired-end 101 bp sequences were obtained using the Illumina platform.

Allele-resolved RNA-seq analysis was performed as described by Sakata et al. (2017) with minor modifications: (1) paired-end reads were used as single-end reads; (2) the numbers of allele-specific reads in replicates were summed; (3) genes with more than ten allele-specific reads were considered to be informative for assessing the expression from the Xi; (4) Cufflinks v2.2.1 cuffdiff (Trapnell et al., 2010) with option '–library-type ff-firststrand –multi-read-correct' was used to estimate gene expression level as FPKM in a non-allelic manner. RNA-seq data of MEFs were reported previously (Sakakibara et al., 2018). For each gene, the number of maternal (B6 or 129) and paternal (JF1) allele-specific reads were counted and percentages of total expression from the paternal allele were calculated as %Xi for assessing

the expression from the Xi. During allele-specific analysis, we noticed that the polymorphism of *Tmsb4x* is only a single error-prone indel (one adenine insertion at nine sequential adenines). Therefore, three genes, *Tmsb4x* in addition to *Las1l* and *Dynlt3* (Sakata et al., 2017), were omitted from the subsequent allele-specific analysis. According to a generally accepted threshold (Peeters et al., 2014), genes with ≥10% of total expression from the Xi in wild type were classified as escapees. To distinguish repressed genes from derepressed genes in non-escapees, we set 10% of total expression from the Xi as a threshold. For comparison among cell lines, only genes with informative %Xi in all cell lines to be compared were considered. For Fig. S1D, genes with FPKM≥1 were considered to be expressed. The expression profile of ESCs was derived from the average of three replicates of the female ESC line CBMS1 in our recent publication (Takahashi et al., 2019).

Western blotting

EpiSCs free from feeder cells were suspended in RIPA buffer/1× protease inhibitor cocktail and placed on ice for 10 min. Following centrifugation at 15,000 rpm (20,400 g) for 10 min at 4°C, the supernatant was collected. SDS-PAGE and immunoreactions were carried out using standard protocols. Images were taken with an ImageQuant LAS 500 (GE Healthcare Life Sciences). The signal intensities of each band were quantified using the ImageJ Gels tool and normalized by dividing the values of respective bands representing either H3K27me3 or H2AK119ub with the value of the band representing histone H3 in each sample.

ChIP and allele-resolved ChIP-seq

For ChIP-qPCR, MEFs and EpiSCs were fixed with DMEM containing 5% formaldehyde. Preparation of chromatin and immunoprecipitation using an antibody against H3K27me3 were carried out as previously described (Nozawa et al., 2013). The primers used for ChIP-qPCR are shown in Table S2. Welch's *t*-test was conducted using R.

For ChIP-seq, following chromatin immunoprecipitation using antibodies against either H3K27me3 or H3K9me3, libraries were generated using the NEBNext Ultra II DNA Library Prep Kit (New England Biolabs) according to the manufacturer's instructions. Size fractionation was carried out to enrich fragments of 100-300 bp from purified DNA for library preparation as well as the library around the size of 200 bp fragments after PCR amplification using AMPure XP (Beckman Coulter) magnetic beads. Each library thus size-fractionated was quantified using a LabChip GX (Perkin Elmer). Libraries were pooled and sequenced on the Illumina HiSeq 3000 to produce 100 bp paired-end reads.

Analysis of allele-resolved ChIP-seq datasets

Paired-end reads were trimmed to remove adaptor sequences using cutadapt (Martin, 2011) and FLASH2 (Magoc and Salzberg, 2011) before mapping, and those with ≥50 bp were used as single-end reads for further analysis. The trimmed reads were mapped to the B6-129S1/JF1 strain-specific diploid genome as described by Sakata et al. (2017) using bwa samse (Li and Durbin, 2009). The custom reference genome included the chromosomes of JF1, the X chromosome of 129S1 and the B6 mm9 reference genome. The mapped positions were converted to mm9 genomic coordinates keeping the strain origin because our custom reference genome incorporated indels in addition to SNPs. The mapping quality was recalculated to be equivalent to the haploid reference by counting the number of suboptimal hits per haploid genome, as the diploid genome has twice as many suboptimal alignments as those on the haploid genome (Miura et al., 2020). Reads with low mapping quality (<20) were discarded to ensure that reads mapped to unique genomic positions were considered with confidence. Possible PCR duplicates were removed using samtools (Li et al., 2009). As a result, each mapped read had a single coordinate of the mm9 reference and a set of possible strain origins.

Note that, for the cell lines used in this study, the genomic sequence of the 129 strain was retained in the vicinity of the mutated *Xist* locus even after extensive backcrosses into the B6 background, and not all autosomal regions were B6/JF1 hybrid owing to the derivation of the F2 generation (see Fig. 1A). Therefore, the haplotype of each cell line was required to assign the

parental origin of a read using a set of possible strain origins at each SNP/ indel site. The haplotypes of chromosome X were inferred as described previously (Sakata et al., 2017). For the autosomal haplotypes, regions with B6/JF1 hybrid were roughly determined by the ratio of JF1-allele to total allele-specific read counts for each 500 kb bin in the input sample, and the boundaries between hybrid and non-hybrid regions were inferred by visual inspection of the distribution of JF1-specific reads in the input and the ChIP samples. Using the haplotype for each cell line, we counted maternal-specific, paternal-specific and total mapped reads separately in the ChIP and input samples in non-overlapping bins across the chromosome and expressed them as RPKM. We calculated the enrichment ratio of the ChIP sample to the corresponding input defined as $\log2[(\text{ChIP RPKM})/(\text{input RPKM})]$. Bins with RPKM<0.1 for total mapped reads and RPKM<0.02 for parental-specific reads were excluded as unmappable. To facilitate direct comparison of the distribution of the histone modification between the cell lines, each profile of the ChIP enrichment was normalized to that of wild-type MEF so that the mode of the difference between the two autosomal profiles was 0. For each histone modification in each cell line, a single normalization factor was determined using the non-allelic profile of autosomal 50 kb bins and applied to any profiles regardless of chromosome, bin size or parental origin. The mode was estimated by the R package 'modeest'.

We used the UCSC genome browser to visualize ChIP enrichments on genomic coordinates (Kent et al., 2002) with scales indicated in each track and the window option 'mean'. To avoid interpreting unmappable bins as unenriched, those ChIP enrichments were estimated by linear interpolation in the case of a single unmappable bin flanked by mappable bins. Otherwise, in the case of successive unmappable bins, we filled those bins with pale gray in all figures. To analyze the ChIP enrichment for each X-linked gene, we defined its gene body as a bin and excluded its length <1 kb due to low read counts. Domains enriched with H3K9me3 or H3K27me3 were called with Enriched Domain Detector (EDD) v1.1.19 (Lund et al., 2014). To allow comparison between different cell lines and between different alleles, we used normalized log(ChIP/Input) profiles as inputs, fixed parameters (bin_size=50, gap_penalty=30), and the score threshold defined as that with FDR<0.05 in wild-type MEF for each H3K9me3 and H3K27me3. The alluvial diagrams were generated using the R package 'ggalluvial'.

Published allele-specific ChIP-seq data for H3K27me3 and H2AK119ub in EBs (GSE135389; Colognori et al., 2020) were processed as described above using Cast and 129S1 SNPs/indels. The PC1 values of Hi-C data in EBs (GSE99991; Wang et al., 2018) were downloaded from Gene Expression Omnibus.

Author contributions
Conceptualization: T. Sado; Methodology: S.I., K.N., T. Sado; Validation: S.I., K.N., T. Sakaguchi, T. Sado; Formal analysis: S.I., K.N., C.O., T. Sado; Investigation: S.I., K.N., C.O., T. Sado; Resources: S.I., T. Sakaguchi, T. Sado; Data curation: S.I., K.N., T. Sado; Writing - original draft: S.I., K.N., T. Sado; Writing - review & editing: S.I., K.N., T. Sado; Visualization: S.I., K.N., T. Sado; Supervision: T. Sado; Project administration: T. Sado; Funding acquisition: K.N., C.O., T. Sado.

Data availability
The allele-specific RNA-seq and ChIP-seq data generated in this study have been deposited in the NCBI Gene Expression Omnibus (GEO) database under accession number GSE201189.

Peer review history
The peer review history is available online at https://journals.biologists.com/dev/ article-lookup/doi/10.1242/dev.200864.

References

Blewitt, M. E., Gendrel, A.-V., Pang, Z., Sparrow, D. B., Whitelaw, N., Craig, J. M., Apedaile, A., Hilton, D. J., Dunwoodie, S. L., Brockdorff, N. et al. (2008). SmcHD1, containing a structural-maintenance-of-chromosomes hinge domain, has a critical role in X inactivation. *Nat. Genet.* **40**, 663-669. doi:10.1038/ng.142

Borsani, G., Tonlorenzi, R., Simmler, M. C., Dandolo, L., Arnaud, D., Capra, V., Grompe, M., Pizzuti, A., Muzny, D., Lawrence, C. et al. (1991). Characterization of a murine gene expressed from the inactive X chromosome. *Nature* **351**, 325-329. doi:10.1038/351325a0

Brideau, N. J., Coker, H., Gendrel, A.-V., Siebert, C. A., Bezstarosti, K., Demmers, J., Poot, R. A., Nesterova, T. B. and Brockdorff, N. (2015). Independent Mechanisms Target SMCHD1 to Trimethylated Histone H3 Lysine 9-Modified Chromatin and the Inactive X Chromosome. *Mol. Cell. Biol.* **35**, 4053-4068. doi:10.1128/MCB.00432-15

Brockdorff, N., Ashworth, A., Kay, G. F., Cooper, P., Smith, S., McCabe, V. M., Norris, D. P., Penny, G. D., Patel, D. and Rastan, S. (1991). Conservation of position and exclusive expression of mouse Xist from the inactive X chromosome. *Nature* **351**, 329-331. doi:10.1038/351329a0

Brons, G. I. M., Smithers, L. E., Trotter, M. W. B., Rugg-Gunn, P., Sun, B., Chuva de Sousa Lopes, S. M., Howlett, S. K., Clarkson, A., Ahrlund-Richter, L., Pedersen, R. A. et al. (2007). Derivation of pluripotent epiblast stem cells from mammalian embryos. *Nature* **448**, 191-195. doi:10.1038/nature05950

Chadwick, B. P. and Willard, H. F. (2004). Multiple spatially distinct types of facultative heterochromatin on the human inactive X chromosome. *Proc. Natl. Acad. Sci. USA* **101**, 17450-17455. doi:10.1073/pnas.0408021101

Chaumeil, J., Waters, P. D., Koina, E., Gilbert, C., Robinson, T. J. and Graves, J. A. M. (2011). Evolution from XIST-independent to XIST-controlled X-chromosome inactivation: epigenetic modifications in distantly related mammals. *PLoS ONE* **6**, e19040. doi:10.1371/journal.pone.0019040

Chen, G., Schell, J. P., Benitez, J. A., Petropoulos, S., Yilmaz, M., Reinius, B., Alekseenko, Z., Shi, L., Hedlund, E., Lanner, F. et al. (2016). Single-cell analyses of X chromosome inactivation dynamics and pluripotency during differentiation. *Genome Res.* **26**, 1342-1354. doi:10.1101/gr.201954.115

Colognori, D., Sunwoo, H., Wang, D., Wang, C.-Y. and Lee, J. T. (2020). Xist repeats A and B account for two distinct phases of X inactivation establishment. *Dev. Cell* **54**, 21-32.e5. doi:10.1016/j.devcel.2020.05.021

Erhardt, S., Su, I.-H., Schneider, R., Barton, S., Bannister, A. J., Perez-Burgos, L., Jenuwein, T., Kouzarides, T., Tarakhovsky, A. and Surani, M. A. (2003). Consequences of the depletion of zygotic and embryonic enhancer of zeste 2 during preimplantation mouse development. *Development* **130**, 4235-4248. doi:10.1242/dev.00625

Fang, J., Chen, T., Chadwick, B., Li, E. and Zhang, Y. (2004). Ring1b-mediated h2a ubiquitination associates with inactive X chromosomes and is involved in initiation of X inactivation. *J. Biol. Chem.* **279**, 52812-52815. doi:10.1074/jbc. C400493200

Gdula, M. R., Nesterova, T. B., Pintacuda, G., Godwin, J., Zhan, Y., Ozadam, H., McClellan, M., Moralli, D., Krueger, F., Green, C. M. et al. (2019). The non-canonical SMC protein SmcHD1 antagonises TAD formation and compartmentalisation on the inactive X chromosome. *Nat. Commun.* **10**, 30. doi:10.1038/s41467-018-07907-2

Gendrel, A.-V., Apedaile, A., Coker, H., Termanis, A., Zvetkova, I., Godwin, J., Tang, Y. A., Huntley, D., Montana, G., Taylor, S. et al. (2012). Smchd1-dependent and -independent pathways determine developmental dynamics of CpG island methylation on the inactive X chromosome. *Dev. Cell* **23**, 265-279. doi:10.1016/j.devcel.2012.06.011

Gendrel, A.-V. V., Tang, Y. A., Suzuki, M., Godwin, J., Nesterova, T. B., Greally, J. M., Heard, E. and Brockdorff, N. (2013). Epigenetic functions of smchd1 repress gene clusters on the inactive X chromosome and on autosomes. *Mol. Cell. Biol.* **33**, 3150-3165. doi:10.1128/MCB.00145-13

Hoki, Y., Kimura, N., Kanbayashi, M., Amakawa, Y., Ohhata, T., Sasaki, H. and Sado, T. (2009). A proximal conserved repeat in the Xist gene is essential as a genomic element for X-inactivation in mouse. *Development* **136**, 139-146. doi:10. 1242/dev.026427

Jansz, N., Keniry, A., Trussart, M., Bildsoe, H., Beck, T., Tonks, I. D., Mould, A. W., Hickey, P., Breslin, K., Iminitoff, M. et al. (2018a). Smchd1 regulates long-range chromatin interactions on the inactive X chromosome and at Hox clusters. *Nat. Struct. Mol. Biol.* **25**, 766-777. doi:10.1038/s41594-018-0111-z

Jansz, N., Nesterova, T., Keniry, A., Iminitoff, M., Hickey, P. F., Pintacuda, G., Masui, O., Kobelke, S., Geoghegan, N., Breslin, K. A. et al. (2018b). Smchd1 targeting to the inactive X is dependent on the Xist-HnrnpK-PRC1 pathway. *Cell Rep.* **25**, 1912-1923.e9. doi:10.1016/j.celrep.2018.10.044

Kalantry, S. and Magnuson, T. (2006). The polycomb group protein EED is dispensable for the initiation of random X-chromosome inactivation. *PLoS Genet.* **2**, e66. doi:10.1371/journal.pgen.0020066

Kalantry, S., Mills, K. C., Yee, D., Otte, A. P., Panning, B. and Magnuson, T. (2006). The Polycomb group protein Eed protects the inactive X-chromosome from differentiation-induced reactivation. *Nat. Cell Biol.* **8**, 195-202. doi:10.1038/ncb1351

Keniry, A., Gearing, L. J., Jansz, N., Liu, J., Holik, A. Z., Hickey, P. F., Kinkel, S. A., Moore, D. L., Breslin, K., Chen, K. et al. (2016). Setdb1-mediated H3K9 methylation is enriched on the inactive X and plays a role in its epigenetic silencing. *Epigenet. Chromatin.* **9**, 16. doi:10.1186/s13072-016-0064-6

Kent, W. J., Sugnet, C. W., Furey, T. S., Roskin, K. M., Pringle, T. H., Zahler, A. M. and Haussler, D. (2002). The Human Genome Browser at UCSC. *Genome Res.* **12**, 996-1006. doi:10.1101/gr.229102

Kojima, Y., Kaufman-Francis, K., Studdert, J. B., Steiner, K. A., Power, M. D., Loebel, D. A. F., Jones, V., Hor, A., de Alencastro, G., Logan, G. J. et al. (2014). The transcriptional and functional properties of mouse epiblast stem cells resemble the anterior primitive streak. *Cell Stem Cell* **14**, 107-120. doi:10.1016/j.stem.2013.09.014

Leong, H. S., Chen, K., Hu, Y., Lee, S., Corbin, J., Pakusch, M., Murphy, J. M., Majewski, I. J., Smyth, G. K., Alexander, W. S. et al. (2013). Epigenetic regulator Smchd1 functions as a tumor suppressor. *Cancer Res.* **73**, 1591-1599. doi:10.1158/0008-5472.CAN-12-3019

Li, H. and Durbin, R. (2009). Fast and accurate short read alignment with Burrows–Wheeler transform. *Bioinformatics* **25**, 1754-1760. doi:10.1093/bioinformatics/btp324

Li, H., Handsaker, B., Wysoker, A., Fennell, T., Ruan, J., Homer, N., Marth, G., Abecasis, G. and Durbin, R. (2009). The Sequence Alignment/Map format and SAMtools. *Bioinformatics* **25**, 2078-2079. doi:10.1093/bioinformatics/btp352

Lund, E., Oldenburg, A. R. and Collas, P. (2014). Enriched domain detector: a program for detection of wide genomic enrichment domains robust against local variations. *Nucleic Acids Res.* **42**, e92-e92. doi:10.1093/nar/gku324

Lyon, M. F. (1961). Gene Action in the X-chromosome of the Mouse (Mus musculus L.). *Nature* **190**, 372-373. doi:10.1038/190372a0

Magoc, T. and Salzberg, S. L. (2011). FLASH: fast length adjustment of short reads to improve genome assemblies. *Bioinformatics* **27**, 2957-2963. doi:10.1093/bioinformatics/btr507

Marahrens, Y., Panning, B., Dausman, J., Strauss, W. and Jaenisch, R. (1997). Xist-deficient mice are defective in dosage compensation but not spermatogenesis. *Genes Dev.* **11**, 156-166. doi:10.1101/gad.11.2.156

Martin, M. (2011). Cutadapt removes adapter sequences from high-throughput sequencing reads. *Embnet J* **17**, 10-12. doi:10.14806/ej.17.1.200

Miura, H., Takahashi, S., Shibata, T., Nagao, K., Obuse, C., Okumura, K., Ogata, M., Hiratani, I. and Takebayashi, S.-I. (2020). Mapping replication timing domains genome wide in single mammalian cells with single-cell DNA replication sequencing. *Nat. Protoc.* **15**, 4058-4100. doi:10.1038/s41596-020-0378-5

Mohandas, T., Sparkes, R. S. and Shapiro, L. J. (1981). Reactivation of an inactive human X chromosome: evidence for X inactivation by DNA methylation. *Science* **211**, 393-396. doi:10.1126/science.6164095

Montgomery, N. D., Yee, D., Chen, A., Kalantry, S., Chamberlain, S. J., Otte, A. P. and Magnuson, T. (2005). The murine polycomb group protein Eed is required for global histone H3 lysine-27 methylation. *Curr. Biol.* **15**, 942-947. doi:10.1016/j.cub.2005.04.051

Napoles, M., de Mermoud, J. E., Wakao, R., Tang, Y. A., Endoh, M., Appanah, R., Nesterova, T. B., Silva, J., Otte, A. P., et al. (2004). Polycomb group proteins Ring1A/B link ubiquitylation of histone H2A to heritable gene silencing and X inactivation. *Dev. Cell* **7**, 663-676. doi:10.1016/j.devcel.2004.10.005

Nesterova, T. B., Wei, G., Coker, H., Pintacuda, G., Bowness, J. S., Zhang, T., Almeida, M., Bloechl, B., Moindrot, B., Carter, E. J. et al. (2019). Systematic allelic analysis defines the interplay of key pathways in X chromosome inactivation. *Nat. Commun.* **10**, 3129. doi:10.1038/s41467-019-11171-3

Nozawa, R.-S., Nagao, K., Igami, K.-T., Shibata, S., Shirai, N., Nozaki, N., Sado, T., Kimura, H. and Obuse, C. (2013). Human inactive X chromosome is compacted through a PRC2-independent SMCHD1-HBiX1 pathway. *Nat. Struct. Mol. Biol.* **20**, 566-573. doi:10.1038/nsmb.2532

Peeters, S. B., Cotton, A. M. and Brown, C. J. (2014). Variable escape from X-chromosome inactivation: identifying factors that tip the scales towards expression. *BioEssays* **36**, 746-756. doi:10.1002/bies.201400032

Penny, G. D., Kay, G. F., Sheardown, S. A., Rastan, S. and Brockdorff, N. (1996). Requirement for Xist in X chromosome inactivation. *Nature* **379**, 379131a0. doi:10.1038/379131a0

Peters, A. H. F. M., O'Carroll, D., Scherthan, H., Mechtler, K., Sauer, S., Schöfer, C., Weipoltshammer, K., Pagani, M., Lachner, M., Kohlmaier, A. et al. (2001). Loss of the Suv39h histone methyltransferases impairs mammalian heterochromatin and genome stability. *Cell* **107**, 323-337. doi:10.1016/S0092-8674(01)00542-6

Plath, K., Fang, J., Mlynarczyk-Evans, S. K., Cao, R., Worringer, K. A., Wang, H., de la Cruz, C. C., Otte, A. P., Panning, B. and Zhang, Y. (2003). Role of histone H3 lysine 27 methylation in X inactivation. *Science* **300**, 131-135. doi:10.1126/science.1084274

Rens, W., Wallduck, M. S., Lovell, F. L., Ferguson-Smith, M. A. and Ferguson-Smith, A. C. (2010). Epigenetic modifications on X chromosomes in marsupial and monotreme mammals and implications for evolution of dosage compensation. *Proc. Natl Acad. Sci. USA* **107**, 17657-17662. doi:10.1073/pnas.0910322107

Sado, T. and Sakaguchi, T. (2013). Species-specific differences in X chromosome inactivation in mammals. *Reproduction* **146**, R131-R139. doi:10.1530/REP-13-0173

Sado, T., Okano, M., Li, E. and Sasaki, H. (2004). De novo DNA methylation is dispensable for the initiation and propagation of X chromosome inactivation. *Development* **131**, 975-982. doi:10.1242/dev.00995

Sado, T., Hoki, Y. and Sasaki, H. (2005). Tsix silences Xist through modification of chromatin structure. *Dev. Cell* **9**, 159-165. doi:10.1016/j.devcel.2005.05.015

Sakakibara, Y., Nagao, K., Blewitt, M., Sasaki, H., Obuse, C. and Sado, T. (2018). Role of SmcHD1 in establishment of epigenetic states required for the maintenance of the X-inactivated state in mice. *Development* **145**, dev166462. doi:10.1242/dev.166462

Sakata, Y., Nagao, K., Hoki, Y., Sasaki, H., Obuse, C. and Sado, T. (2017). Defects in dosage compensation impact global gene regulation in the mouse trophoblast. *Development* **144**, 2784-2797. doi:10.1242/dev.149138

Schotta, G., Lachner, M., Sarma, K., Ebert, A., Sengupta, R., Reuter, G., Reinberg, D. and Jenuwein, T. (2004). A silencing pathway to induce H3-K9 and H4-K20 trimethylation at constitutive heterochromatin. *Gene Dev.* **18**, 1251-1262. doi:10.1101/gad.300704

Silva, J., Mak, W., Zvetkova, I., Appanah, R., Nesterova, T. B., Webster, Z., Peters, A. H., Jenuwein, T., Otte, A. P. and Brockdorff, N. (2003). Establishment of histone H3 methylation on the inactive X chromosome requires transient recruitment of Eed-Enx1 polycomb group complexes. *Dev. Cell* **4**, 481-495. doi:10.1016/S1534-5807(03)00068-6

Sugimoto, M., Kondo, M., Koga, Y., Shiura, H., Ikeda, R., Hirose, M., Ogura, A., Murakami, A., Yoshiki, A., Chuva de Sousa Lopes, S. M. et al. (2015). A simple and robust method for establishing homogeneous mouse epiblast stem cell lines by Wnt inhibition. *Stem Cell Rep.* **4**, 744-757. doi:10.1016/j.stemcr.2015.02.014

Takahashi, S., Miura, H., Shibata, T., Nagao, K., Okumura, K., Ogata, M., Obuse, C., Takebayashi, S.-I. and Hiratani, I. (2019). Genome-wide stability of the DNA replication program in single mammalian cells. *Nat. Genet.* **51**, 529-540. doi:10.1038/s41588-019-0347-5

Tesar, P. J., Chenoweth, J. G., Brook, F. A., Davies, T. J., Evans, E. P., Mack, D. L., Gardner, R. L. and McKay, R. D. G. (2007). New cell lines from mouse epiblast share defining features with human embryonic stem cells. *Nature* **448**, 196-199. doi:10.1038/nature05972

Trapnell, C., Williams, B. A., Pertea, G., Mortazavi, A., Kwan, G., van Baren, M. J., Salzberg, S. L., Wold, B. J. and Pachter, L. (2010). Transcript assembly and quantification by RNA-Seq reveals unannotated transcripts and isoform switching during cell differentiation. *Nat. Biotechnol.* **28**, 511-515. doi:10.1038/nbt.1621

Wang, J., Mager, J., Chen, Y., Schneider, E., Cross, J. C., Nagy, A. and Magnuson, T. (2001). Imprinted X inactivation maintained by a mouse Polycomb group gene. *Nat. Genet.* **28**, ng574. doi:10.1038/ng574

Wang, C.-Y., Jégu, T., Chu, H.-P., Oh, H. J. and Lee, J. T. (2018). SMCHD1 merges chromosome compartments and assists formation of super-structures on the inactive X. *Cell* **174**, 406-421.e25. doi:10.1016/j.cell.2018.05.007

Wang, C.-Y. Y., Colognori, D., Sunwoo, H., Wang, D. and Lee, J. T. (2019). PRC1 collaborates with SMCHD1 to fold the X-chromosome and spread Xist RNA between chromosome compartments. *Nat. Commun.* **10**, 2950. doi:10.1038/s41467-019-10755-3

Zakharova, I. S., Shevchenko, A. I., Shilov, A. G., Nesterova, T. B., VandeBerg, J. L. and Zakian, S. M. (2011). Histone H3 trimethylation at lysine 9 marks the inactive metaphase X chromosome in the marsupial Monodelphis domestica. *Chromosoma* **120**, 177-183. doi:10.1007/s00412-010-0300-y

Żylicz, J. J., Bousard, A., Žumer, K., Dossin, F., Mohammad, E., da Rocha, S. T. T., Schwalb, B., Syx, L., Dingli, F., Loew, D. et al. (2019). The implication of early chromatin changes in X chromosome inactivation. *Cell* **176**, 182-197.e23. doi:10.1016/j.cell.2018.11.041